

UNIVERSITÀ DEGLI STUDI DI GENOVA

SCUOLA POLITECNICA

DICCA

CITY UNIVERSITY LONDON

SCHOOL OF ENGINEERING AND MATHEMATICAL
SCIENCES



Control of
bluff bodies' wake
using flexible filaments

Author:

Edoardo Alinovi

Supervisors:

Prof. Alessandro Bottaro

Prof. Alfredo Pinelli

Co-supervisor:

Dr. Mohammad Omidyeganeh

July 2014

Acknowledgement / Ringraziamenti

I would like to thank Professor Alessandro Bottaro for giving me the possibility to write my thesis at City University London and for having proposed me this interesting topic.

I am very grateful to Professor Alfredo Pinelli and Dr. Mohammad Omidyeganeh, they accepted me at City University London and they always make me feel part of their research group. I really appreciate their patience and their support during this months; I am really proud of the work that we carried out together, thanks.

Grazie a Marco, cercavo un compagno di stanza ed invece ho trovato un vero amico.

Un grazie di cuore alla mia famiglia, mia madre, mio padre, mio fratello Riccardo e i nonni, per il loro supporto durante questi anni di studio. Mi hanno sempre spinto a dare il massimo e sono loro molto grato.

Grazie ad Erica, che riempie le mie giornate con il suo bellissimo sorriso.

Sommario

Numerosi esseri viventi traggono vantaggio da appendici flessibili che, muovendosi attivamente o passivamente nel fluido circostante, generano movimento o portano ad un miglioramento delle prestazioni aerodinamiche. La natura è ricca di esempi: alcuni batteri usano i loro flagelli per muoversi nel fluido in quiete, mentre gli uccelli usano le loro piume per controllare il flusso durante il volo, aumentando così le prestazioni aerodinamiche e abbassando l'energia necessaria al volo.

Una comprensione più approfondita delle interazioni fluido-struttura può portare ad applicazioni ingegneristiche che sono basate sull'imitazione della natura e ottenere così un miglioramento delle tecnologie odierne.

Il presente lavoro di tesi è mirato alla simulazione delle complesse interazioni fluido-struttura a cui sono sottoposti una serie di filamenti flessibili ed inestensibili, incernierati al bordo di uscita di un cilindro tridimensionale. Il cilindro è il prototipo più semplice di corpo tozzo, notoriamente affetto da scarse prestazioni aerodinamiche a causa del massiccio distacco dello strato limite ed alla creazione di una larga zona di ricircolo; ispirandosi alla natura, la presenza dei filamenti potrebbe portare ad un sensibile miglioramento della aerodinamica del corpo.

La ricerca è effettuata tramite simulazioni numeriche. Le equazioni di governo del moto del fluido sono discretizzate su una griglia collocata e risolte mediante un codice ai volumi finiti, mentre i filamenti sono modellizzati mediante equazioni proprie della meccanica delle strutture. L'accoppiamento tra fluido e struttura viene effettuato utilizzando il metodo dei contorni immersi, che evita l'uso di griglie mobili o deformabili conformanti ai corpi flessibili. Il codice è stato validato utilizzando numerosi casi disponibili in letteratura, trovando un ottimo riscontro con gli altri autori.

Le simulazioni sono tutte effettuate al di là della soglia di tridimensionalità del flusso in modo che i filamenti siano indotti a muoversi in ogni direzione da un flusso completamente tridimensionale.

Sono state testate differenti configurazioni dei filamenti e diversi parametri; le prestazioni aerodinamiche del corpo sono state confrontate con il cilindro privo di appendici, riscontrando, in tutti i casi simulati, un netto miglioramento dei coefficienti aerodinamici.

L'effetto dei filamenti sulla struttura della scia è stato preso in considerazione, osservando, a seconda delle configurazioni, un anticipo della seconda biforcazione tridimensionale o la soppressione della prima instabilità tridimensionale.

Abstract

Numerous living beings take advantage of flexible appendages that, moving actively or passively in the surrounding fluid, generate locomotion or lead to an amelioration of the aerodynamic performance. Nature is rich of examples: some bacteria use their flagella to move through a quiescent fluid, while the birds use their feathers that, interacting with the flow, increase their aerodynamic performance, decreasing the energy needed to fly.

Improved understating of the fluid-structure interaction can lead to engineering applications that exploit the design principle of Nature and to an improvement of the human technologies.

The present work is aimed to simulate the complex fluid-structure interaction to which flexible, inextensible filaments, clamped in rear of a three-dimensional circular cylinder, are subjected.

The cylinder is the simplest prototype of bluff body, notoriously affected by low aerodynamic performance because of the strong separation of the boundary layer and the generations of a large recirculation zone; inspiring to Nature, the filaments may lead to good improvement of the aerodynamic of the body.

The investigation is carried out through numerical simulations. The governing differential equations of the flow are discretized on a non-staggered grid and solved using a finite volume code, while the filaments are modelled using the theory of the structure mechanics. The coupling between fluid and structure is performed using the immersed boundary method, that avoid the use of moving or deforming grids conforming to the flexible bodies.

The code has been validated using numerous test cases, obtaining very good agreement with the other authors.

The simulations are performed beyond the three-dimensionality threshold such that the filaments are induced to move in each space direction by a fully developed three-dimensional flow. Different configurations of the the filaments and parameters have been tested; the aerodynamic performance of the body has been compared with the bare cylinder, noting an improvement of the aerodynamic coefficients for all the cases tested.

The effect of the filaments on the wake structure has been visualized and, in function of the case tested, an anticipation of the second three-dimensional bifurcation or an inhibition of the first shedding mode has been observed.

Contents

1	Introduction	1
1.1	Review of Vortex Dynamics in a Cylinder Wake	2
1.2	Case of Study	5
2	Numerical Method	6
2.1	The Navier-Stokes Equations	6
2.1.1	Non-Dimensionalization of the Navier-Stokes Equations	7
2.2	Finite Volume Method	8
2.3	Fractional Step Method	12
2.4	Immersed Boundary Method	14
2.4.1	Mathematical formulation	14
2.4.2	Interpolation and Convolution	15
2.4.3	Numerical Implementation	17
2.5	Filament Governing Equations	20
2.5.1	Non-dimensionalization of the Equations	21
2.6	Discretisation of the Filament Equation	21
2.6.1	Time And Space Discretisation	21
2.7	Boundary Conditions	22
2.7.1	Fixed end	22
2.7.2	Free end	23
2.8	Numerical Resolution of Filament's Equation	24
3	Validation	25
3.1	Validation Of The Filament Model	26
3.2	Single Filament in a Uniform Flow	28
3.3	Hinged Filament behind a 2D Circular Cylinder	31
4	Results	33
4.1	Computational Domain	34
4.2	Choice of the Bending Stiffness	36
4.3	Simulation Cases: $L/D = 1$	37
4.3.1	Dynamics of the Filaments behind the Cylinder	38
4.3.2	Effect On The Cylinder Wake	44
4.3.3	Effect on the Aerodynamic Coefficients	47
4.4	Simulation cases: $L/D = 0.5$	50
4.4.1	Dynamics of the Filaments behind the Cylinder	50
4.4.2	Effect on the Aerodynamic Coefficients	52

4.4.3 Other simulations	52
5 Conclusions	56
Bibliografia	59

Chapter 1

Introduction

Fluid-structure interactions are commonplace in nature. Swimming fish and several micro-organisms base their locomotion on complex interaction between their deformable bodies and the surrounding fluid. Other living beings, despite not having active mechanisms of locomotion, take advantage of appendages moving passively in the flow to increase their aerodynamic performance and to decrease the energy needed to move. This interesting feature can be found in the birds' feathers that, acting on the flow, produce an amelioration of aerodynamic performance.

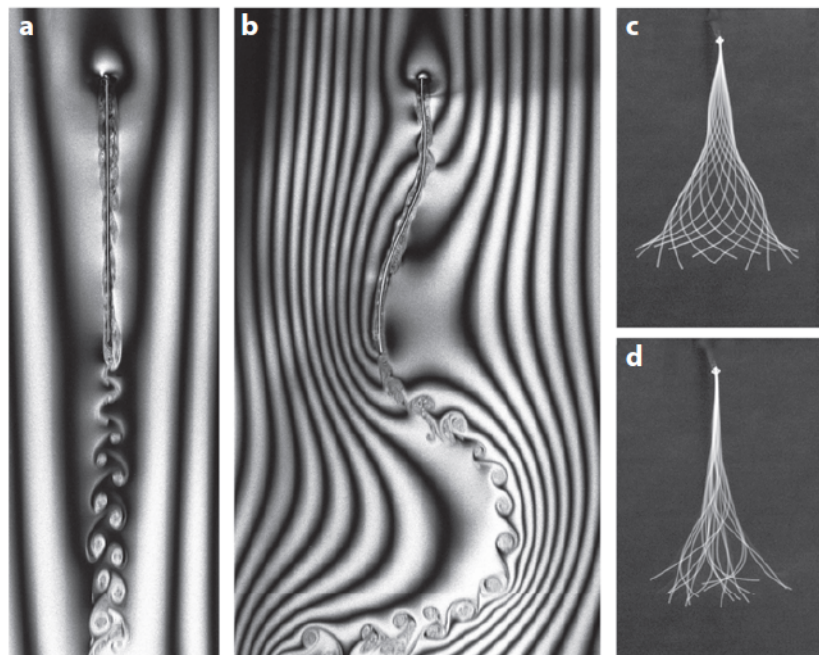


Figure 1.1: Filament immersed in a soap film: (a) stretched state. (b) flapping state. (c) flapping filament at several time points along its flapping cycle. (d) The same filament at higher flow speed, showing aperiodic flapping.

Biomimetics is the branch of science that studies the living beings in nature as source of inspiration for the improvement of human technologies. Mechanisms based on the interaction between flexible bodies and fluid flow are increasing their importance in engineering applications and several researchers focused their attention on these problems. On one hand, the knowledge of the physical mechanisms

involved in these interactions can lead to a better understanding of some basic biological processes and inspire new technologies. On the other hand, modelling these phenomena is a challenge because of their complex geometry and freely moving boundaries which give rise to complicated fluid dynamics.

The first experiments on a flexible filaments moving in a uniform flow, shown in figure 1.1, was performed by Zhang et al.[1]. They visualized the motion of the filaments in a two dimensional soap film and figured out the complex dynamic that can arise from the interaction between the fluid and the immersed bodies. They showed two distinct stable states for a single filament (see figure 1.1): the stretched state and a self sustained flapping state. Inspired by the experiments, Peskin et al. [2] performed numerical simulations on the filament-fluid interaction problem and found that the mass of the filament plays an important role in the dynamics of flapping.

Bagheri et al. [3] studied the dynamics of a flexible filament free to flap in the wake of a two dimensional circular cylinder. They found a symmetry breaking with the filament oscillating in the upper or in the lower part of the cylinder. This behaviour is associated to a net generation of lift and torque; a decrease in drag was also observed.

As outlined in the above examples, the presence of flexible bodies can lead to interesting dynamics and produce aerodynamic advantages. In the present work, the circular cylinder will be taken as a prototype of a bluff body and numerical simulations will be performed with the aim of discovering the effects of flexible filaments clamped in the rear of the cylinder. In the next section a short review of vortex dynamic in the cylinder wake and flow regimes will be proposed.

1.1 Review of Vortex Dynamics in a Cylinder Wake

The vortex dynamics in a cylinder wake presents numerous bifurcations and the structure of the wake is significantly different depending on the flow regime considered. The Reynolds number, $Re = \frac{UD}{\nu}$, is the main bifurcation parameter and in correspondence of certain value of Re the following regimes can arise:

- $Re < 49$: at Re below around 49, as shown in figure 1.2, the wake comprises a steady recirculation region of two symmetrically placed vortices on each side of the wake whose length grows as the Reynolds number increases.

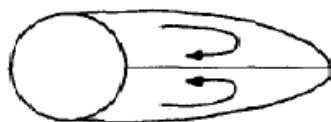


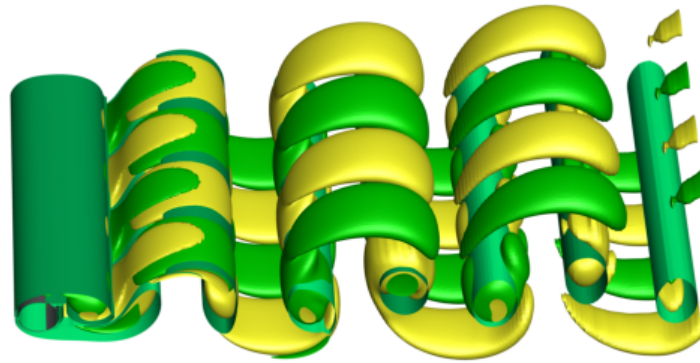
Figure 1.2: Steady wake behind a circular cylinder at low Re .

- $49 < Re < 190$: The recirculation region develops instabilities whose strength and amplification grow with Re . There is the manifestation of a repeating pattern of swirling vortices (Von Karman street) caused by the unsteady separation of the flow around the cylinder. The wake oscillations are purely periodic over the this range and cause the oscillation of the forces over the cylinder.



Figure 1.3: Unsteady wake behind a circular cylinder after the first bifurcation.

- $190 < Re < 260$: This regime is associated with two discontinuous changes in the wake formation as Re is increased. The flow becomes three dimensional and two different shedding modes occurs, namely mode A and mode B. The mode A instability, as shown in figure 1.4, is characterized by the formation of primary vortex loop that becomes stretched into streamwise vortex pairs of wavelength about $\frac{\lambda}{D} \approx 4$ in the spanwise direction.



(a)



(b)

Figure 1.4: Wake structure for a three dimensional circular cylinder at $Re = 200$: iso-surface of positive (green) and negative (yellow) streamwise vorticity; in dark green and light blue iso-surface of negative and positive spanwise vorticity are shown.

The mode B changes the shape of the wake and presents a finer scale streamwise vortex pairs of spanwise wavelength of about $\frac{\lambda}{D} \approx 1$ (see figure 1.5).

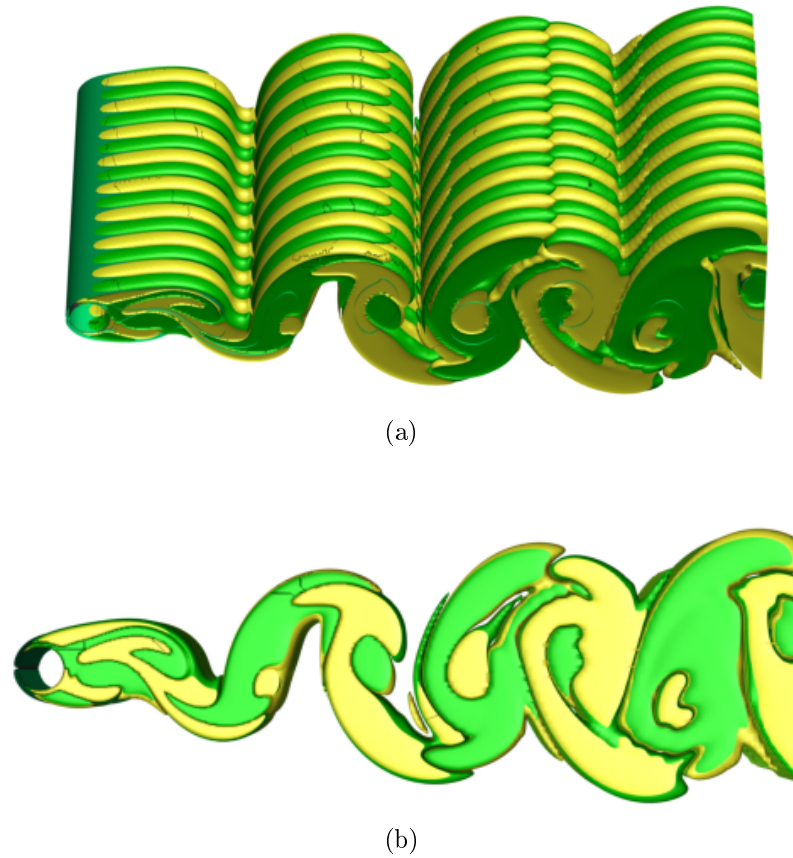


Figure 1.5: Wake structure for a three dimensional circular cylinder at $Re = 270$: iso-surface of positive (green) and negative (yellow) streamwise vorticity; in dark green and light blue iso-surface of negative and positive spanwise vorticity are shown.

After $Re = 260$ there is an increase in disorder and the flow begins to become turbulent. Sever bifurcation and changes in the wake of the cylinder occur and some of these are not fully understood. Their description is beyond the scope of this work and more information can be found in [4].

1.2 Case of Study

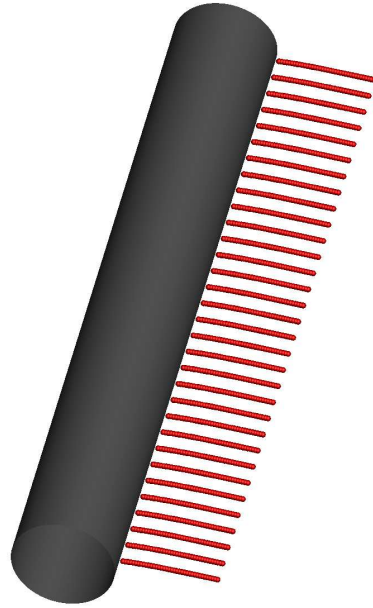


Figure 1.6: Cylinder equipped with flexible filaments.

The present work has the aim to simulate the dynamic of flexible, inextensible filaments clamped in the rear of a three dimensional circular cylinder and analyse the effect that their presence have in the flow; a sketch of the filaments arrangement is proposed in figure 1.6. The simulations performed are DNS (direct numerical simulation) and the governing equations of the flow are solved directly without any approximation of smaller scales. All the numerical calculations are perform beyond the three dimensionality threshold ($Re = 190$) such that the filaments are exposed to a three dimensional flow field and they are free to move in any space direction.

Different number of the filaments and their length will be tested and the aerodynamic performance of the body will be measured and compared with the cylinder without the appendages.

Chapter 2

Numerical Method

2.1 The Navier-Stokes Equations

The Navier-Stokes equations, named in honor of Claude-Louis Navier (1785-1836) and George Gabriel Stokes (1819-1903), describes the motion of fluids from a macroscopic point of view, assuming that the fluid can be treated as a continuum (it is infinitely divisible and it is not composed of discrete elements as atoms or molecules).

The equations, in their most complete form, are nonlinear, coupled partial differential equations and their analytical resolution is often complex or not possible. Only in few particular cases, involving simple geometries and special boundary conditions, an analytical solution can be found. These flows are important to study the fundamentals of fluid mechanics but their practical relevance in engineering and scientific applications is limited. Thus, a numerical approach is needed in order to solve the equations out of those particular situations.

The equations arise from the conservation of momentum and mass for an arbitrary portion of fluid Ω of surface S :

$$\frac{\partial}{\partial t} \int_{\Omega} \rho \mathbf{u} d\Omega + \int_S \rho \mathbf{u} \mathbf{u} \cdot \mathbf{n} dS = \int_S \rho \mathbf{T} \cdot \mathbf{n} dS + \int_{\Omega} \rho \mathbf{f} d\Omega \quad , \quad (2.1)$$

$$\frac{\partial}{\partial t} \int_{\Omega} \rho d\Omega + \int_S \rho \mathbf{u} \cdot \mathbf{n} dS = 0 \quad , \quad (2.2)$$

where \mathbf{u} is the velocity vector, \mathbf{f} represents forces per unit of volume, such as gravity, that may be applied at the fluid, \mathbf{T} is the stress tensor acting on the surface of the fluid volume, \mathbf{n} is the unit vector normal to the surface S and t is the time. The stress tensor \mathbf{T} has its own structure in function of the type of fluid considered.

A simplification of resulting flow governing equations is obtained introducing the following assumption:

- Incompressibility
- Isothermal flow
- Newtonian fluid

The first two assumptions lead to consider as constant the fluid density ρ and the dynamic viscosity μ , that, in general, may vary with space, time and temperature. These simplifications rule out the solvability of high speed flows ($Ma > 0.3$), where the effect of compressibility cannot be neglected, but simplify the solution of a large part of problems in which these proprieties can be considered constant. The third assumption specify the type of fluid and defines the structure of the stress tensor \mathbf{T} that, in cartesian coordinate, becomes:

$$\mathbf{T}_{ij} = -p\delta_{ij} + \mu\left(\frac{\partial u_i}{\partial x_j} + \frac{\partial u_j}{\partial x_i}\right) \quad , \quad (2.3)$$

here x_i stands for the i -th component of the coordinate vector, p is the pressure and δ_{ij} is the Kronecker delta. The stress tensor is therefore composed by two part acting together on the surface of the fluid volume: the first one is related to the pressure and the second one takes into account the viscous stresses contribution.

Using these hypothesis, the general conservation equations for the i -th cartesian component simplify in:

$$\frac{\partial}{\partial t} \int_{\Omega} \rho \mathbf{u} d\Omega + \int_S \rho u_i \mathbf{u} \cdot \mathbf{n} dS = \int_S \mathbf{t}_i \cdot \mathbf{n} dS + \int_{\Omega} \rho f_i d\Omega \quad , \quad (2.4)$$

$$\int_S \mathbf{u} \cdot \mathbf{n} dS = 0 \quad , \quad (2.5)$$

where \mathbf{t}_i is given by:

$$\mathbf{t}_i = -p\mathbf{e}_i + \mu\left(\frac{\partial u_i}{\partial x_j} + \frac{\partial u_j}{\partial x_i}\right)\mathbf{e}_j \quad , \quad (2.6)$$

while \mathbf{e}_i indicates the unit vector in the direction of the coordinate x_i .

Applying to surface integrals the Gauss's divergence theorem and after some manipulations, it is possible to obtain the governing equations in a differential form. The result are the Navier-stokes equations:

$$\frac{\partial \mathbf{u}}{\partial t} + \mathbf{u} \cdot \nabla \mathbf{u} = -\nabla p + \nu \nabla^2 \mathbf{u} + \mathbf{f} \quad (2.7)$$

$$\nabla \cdot \mathbf{u} = 0 \quad (2.8)$$

Both the expressions for conservation equations are valid. The use of the integral formulation is useful when dealing with finite volume method which will be presented in the section 1.2 .

2.1.1 Non-Dimensionalization of the Navier-Stokes Equations

Non-dimensionalization is a common practice in fluid dynamics and consist in scaling the terms of the equations with suitable reference quantities in order to reduce the free parameters in the problem studied. In addition, the non-dimensionalization procedure helps to compare the order of magnitude of various terms and emphasizes the role that some particular parameter plays in the physics of the problem.

The Navier-Stokes equations can be non-dimensionalized introducing the following reference scales:

- Length scale: L_c
- Velocity scale: U_∞
- Pressure: ρU_∞^2
- Time: $\frac{L_c}{U_\infty}$

This choice lead to the asterisk indicating non-dimensional quantities:

$$\mathbf{x}^* = \frac{\mathbf{x}}{L_c}$$

$$\mathbf{u}^* = \frac{\mathbf{u}}{U_\infty}$$

$$p^* = \frac{p}{\rho U_\infty^2}$$

$$t^* = \frac{t L_c}{U_\infty}$$

$$\mathbf{f}^* = \frac{L_c}{U_\infty^2} \mathbf{f}$$

Substituting into equations (2.7)-(2.8), the non-dimensional Navier-Stokes equations read:

$$\frac{\partial \mathbf{u}^*}{\partial t^*} + \mathbf{u}^* \cdot \nabla \mathbf{u}^* = -\nabla p^* + \frac{1}{Re} \nabla^2 \mathbf{u}^* + \mathbf{f}^* \quad (2.9)$$

$$\nabla \cdot \mathbf{u}^* = 0 \quad (2.10)$$

From now on when using these equations the asterisk will be omitted for clarity.

2.2 Finite Volume Method

The finite volume method is a numeric approach for solving compressible and incompressible fluid flows in any number of space dimension.

The starting point are the incompressible Navier-Stokes equations, proposed again below in their non dimensional, differential and cartesian form:

$$\frac{\partial u_i}{\partial t} + u_j \frac{\partial u_i}{\partial x_j} = -\frac{\partial p}{\partial x_j} + \frac{1}{Re} \frac{\partial}{\partial x_j} \frac{\partial u_i}{\partial x_j} + f_i \quad (2.11)$$

$$\frac{\partial u_i}{\partial x_i} = 0 \quad (2.12)$$

The first step towards the solution of the problem is the discretization of the above conservation equations. The fluid domain Ω is subdivided in a finite number of small, non overlapping, control volumes by a grid which defines control volume boundaries.

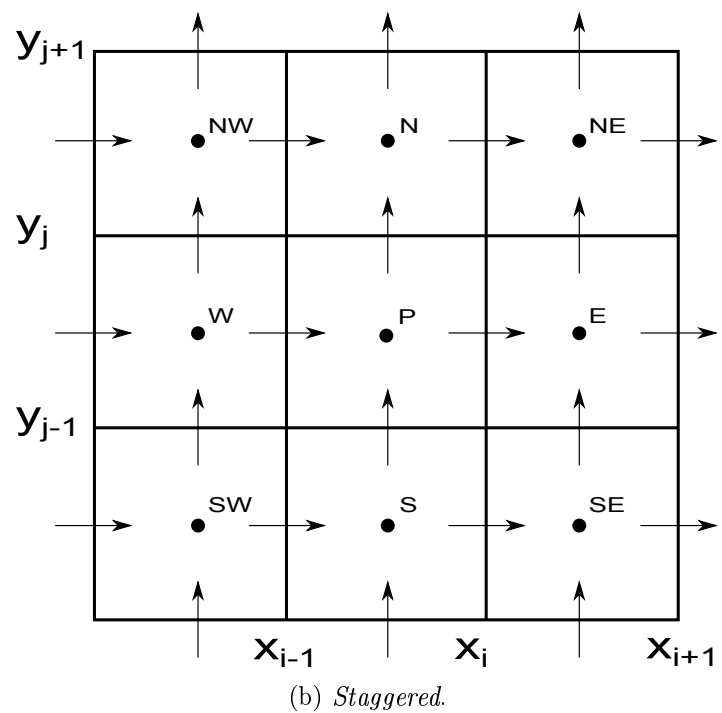
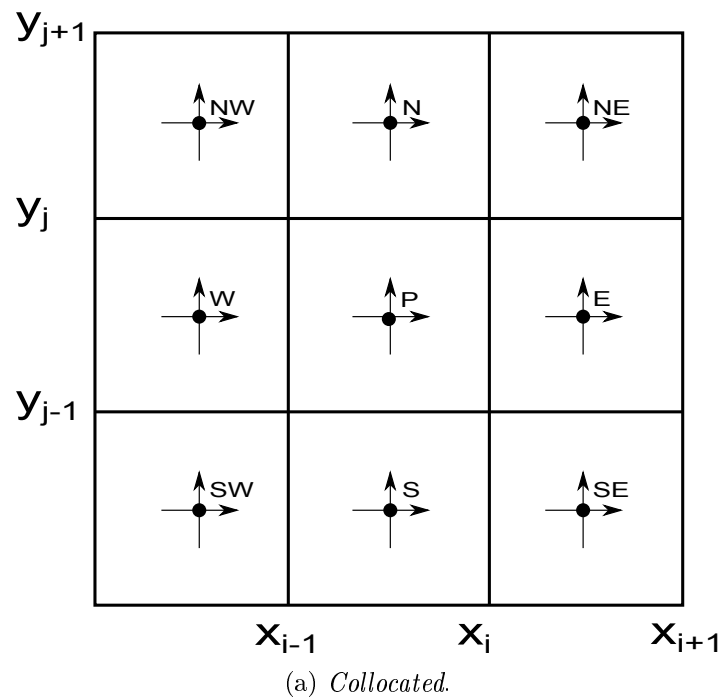


Figure 2.1: Collocated and staggered variables arrangement in a two dimensional grid. x -velocity component is evaluated at \rightarrow , y -velocity component at \uparrow , whereas pressure at \bullet

The computational nodes, where the unknown variables (\mathbf{u} , p) are to be computed, can be arranged mainly in two different ways, as shown in figure 2.1:

- Staggered
- Collocated

The staggered arrangement, allocates the velocities at the control volume boundaries and pressure in the cell centre, while, in the collocated arrangement, all the unknowns are computed in the control volume center. Despite of their simplicity, collocated grids were out of favour for a long time in the past because of their likelihood to create pressure oscillations in the flow field. However, after that solutions at this problem were proposed, the collocated arrangement was preferred thanks to its simplicity in non-cartesian grid generation and memory savings in three-dimensional problems.

The basic idea of the finite volume method is to require the satisfaction of the conservations equations (2.11) at each control volume; thus, if the mass and momentum balance are satisfied at each CV, they will be satisfied on the whole domain. The Navier-Stokes equations and continuity equation are integrated over each control volume assuming the following integral form:

$$\int_{\Omega} \frac{\partial u_i}{\partial t} d\Omega + \int_{\Omega} u_i \frac{\partial u_j}{\partial x_j} d\Omega = - \int_{\Omega} \frac{\partial p}{\partial x_j} d\Omega + \int_{\Omega} \frac{1}{Re} \frac{\partial}{\partial x_j} \frac{\partial u_i}{\partial x_j} d\Omega + \int_{\Omega} f_i d\Omega \quad , \quad (2.13)$$

$$\int_{\Omega} \frac{\partial u_i}{\partial x_i} d\Omega = 0 \quad . \quad (2.14)$$

In figure 2.2 is shown a three-dimensional cartesian control volume together with the notation used. The CV consist of six plane faces, denoted with lower case letters (e,w,n,s,t,b) corresponding to their orientation with respect to the central node (P).

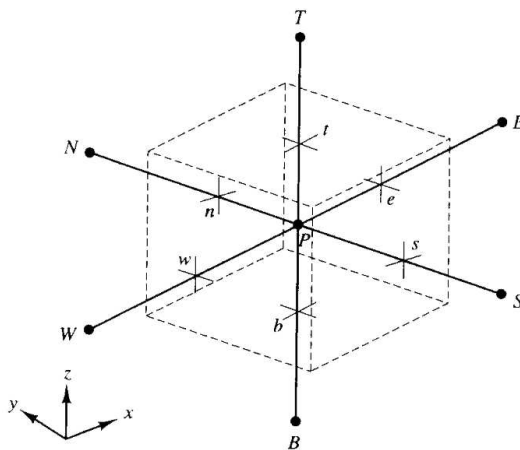


Figure 2.2: Control volume for a 3D cartesian grid

Before proceeding with the numerical approximation, the volume integrals concerning the convecting term and diffusion term can be conveniently transformed in surface integrals over the CV boundary using Gauss' divergence theorem and the incompressibility condition:

$$\int_{\Omega} u_i \frac{\partial u_j}{\partial x_j} d\Omega = \int_S u_i \mathbf{u} \cdot \mathbf{n} dS \quad , \quad (2.15)$$

and

$$\int_{\Omega} \frac{1}{Re} \frac{\partial}{\partial x_j} \frac{\partial u_i}{\partial x_j} d\Omega = \int_S \frac{1}{Re} \nabla u_i \cdot \mathbf{n} dS \quad . \quad (2.16)$$

Here $\nabla = (\frac{\partial}{\partial x}, \frac{\partial}{\partial y}, \frac{\partial}{\partial z})^T$ stands for the gradient operator.

Consider now an arbitrary flux ϕ through the CV boundaries. It can be calculated by the sum of all fluxes through the surface composing the control volume as:

$$\int_S \phi dS = \sum_{k=1}^N \int_{S_k} \phi dS \quad , \quad (2.17)$$

here N is the number of control volume faces and ϕ can be both the convective or diffusive flux defined in equations (2.15)-(2.16). The above expression is still exact and holds for any control volume of arbitrary shape.

The surface integral of ϕ , for an arbitrary face k is estimated with the mid-point rule:

$$\int_{S_k} \phi dS \approx \phi_k S_k \quad . \quad (2.18)$$

The integral is approximated by the value of ϕ at the surface center times the area of the surface at which the integral is calculated. It is possible to show that this approximation is of second order accuracy. Usually, for collocated grids, the value of ϕ at the face center is not known and interpolation is needed in order to express ϕ_k as a function of neighbouring computational nodes. Referring to the figure 2.1(a), the value of ϕ at CV-face center is obtain by linear interpolation between the two nearest nodes, as follows (e.g e face):

$$\Phi_e = \lambda \Phi_P + (1 - \lambda) \Phi_E \quad (2.19)$$

Where λ is a weight defined as:

$$\lambda = \frac{x_e - x_E}{x_E - x_P} \quad (2.20)$$

This scheme is called central difference scheme (CDS) and it is of second order accuracy. For clarity, the discretization of the convective fluxes will be shown only for the e -face of the cartesian CV shown in figure 2.2 and only for the velocity component u in x direction. The fluxes at the other surfaces can be treated in the same fashion applying the appropriate subscripts permutation.

Applying the above approximation, the discrete convective and diffusive flux read:

$$\int_{S_e} u_i \mathbf{u} \cdot \mathbf{n}_e dS_e \approx m_e u_e = m_e [\lambda u_P + (1 - \lambda) u_E] \quad , \quad (2.21)$$

and

$$\int_{S_e} \frac{1}{Re} \nabla u_i \cdot \mathbf{n}_e dS_e \approx \frac{S_e}{Re} \frac{u_E - u_P}{x_E - x_P} \quad . \quad (2.22)$$

$m_e = u_e S_e$ in (2.21) is the mass flow rate through the surface e .

The spatial discretization is completed by the approximation of pressure gradient and body forces, also called source terms. For an arbitrary source term \mathbf{q} the following approximation is applied:

$$\int_{\Omega_P} \mathbf{q} d\Omega \approx \mathbf{q}_P \Delta\Omega_P \quad . \quad (2.23)$$

The integral is estimated by the product between the central value of \mathbf{q} in the control volume center and the cell volume $\Delta\Omega$. This is again a second order accurate approximation.

The finite volume approximation for the pressure term becomes (e.g x direction):

$$\int_{\Omega} \frac{\partial p}{\partial x_j} d\Omega \approx \frac{(p_e - p_w)}{\Delta x_p} \quad (2.24)$$

p_e and p_w are the interpolated values of p at the control volume faces e and w using the already defined central difference scheme.

The forcing term \mathbf{f} :

$$\int_{\Omega_P} \mathbf{f} d\Omega \approx \mathbf{f}_P \Delta\Omega_P \quad . \quad (2.25)$$

After the space discretization, a time advancement strategy is to be defined.

The solution of the Navier-Stokes equations is complicated by the lack of an independent equation for the pressure, whose gradient contributes to each of the three momentum equations. One possibility is to obtain an equation for the pressure by applying the divergence operator to both sides of momentum equation. This approach is called velocity-pressure formulation and it is widely use in solution of the Navier-Stokes equations.

It is worth to note that problems may appear using collocated grids and pressure oscillation may generates in the flow field and leading to unphysical results. The most common approach to avoid this problem was firstly developed by Rhie and Chow [5] and consists in changing the interpolation method used for calculate the mass flow rate m through a control volume surface. The interpolated velocity u_e at a cell face is correct with pressure terms that permit to avoid the problem.

2.3 Fractional Step Method

The fractional step method is a technique to advance in time the fluid flow governing equations and was firstly developed by Chorin [6] and then improved by other authors. The algorithm is based on decomposition of any vector field into a solenoidal part and an irrotational part and, typically, consists of two stages:

- Prediction
- Correction

In the prediction step, the momentum equation is solved, but the resulting solution does not satisfy the continuity equation. In the correction step the previous solution is corrected and the velocity field is projected onto a divergence-free field.

Several numerical implementation are available in the literature; here we will be present the fractional step version employed in the present study and proposed by Kim and Moin [7]. The method is semi-implicit and not all the terms of the momentum equation are discretized in time in the same manner. In particular the second order Crank-Nicolson scheme is used for the wall-normal diffusive term and the second order

Adams-Bashforth scheme for all of the other terms in momentum equation. The two-step time advancement scheme can be written as:

$$\frac{\hat{\mathbf{u}} - \mathbf{u}_i^n}{\Delta t} = -\mathcal{N}_l(\mathbf{u}^n, \mathbf{u}^{n-1}) - \mathcal{G}(\phi^n, \phi^{n-1}) + \frac{1}{Re} \mathcal{L}(\hat{\mathbf{u}}_i, \mathbf{u}^n), \quad (2.26)$$

$$\mathcal{L}\phi = \frac{1}{\Delta t} \mathcal{D}\hat{\mathbf{u}} \quad , \quad (2.27)$$

with:

$$\mathcal{D}(\mathbf{u}^{n+1}) = 0, \quad (2.28)$$

where \mathcal{N}_l is a shorthand notation that include the discretized convective term whose treatment is of no importance and that can be evaluated using the finite volume approach presented in section 1.1. ϕ is a scalar to be determined, \mathcal{L} represents the discrete laplacian operator, and \mathcal{G} and \mathcal{D} the discrete gradient and divergence operator. Equation (2.26) is firstly solved to find the non solenoidal velocity field $\hat{\mathbf{u}}$ and then the equation (2.27) is employed in order to correct the velocity field and satisfy the continuity equation. The projection variable ϕ has the role to enforce the continuity and can be obtained applying the divergence operator to equation (2.26). This operation leads to a Poisson equation for ϕ :

$$\left(\frac{\delta^2}{\delta x_1^2} + \frac{\delta^2}{\delta x_2^2} + \frac{\delta^2}{\delta x_3^2} \right) \phi^{n+1}(i, j, k) = D\hat{\mathbf{u}} = Q(i, j, k) \quad . \quad (2.29)$$

This equation is expressed in its discrete form and can be solved with the classical linear system tools but, especially in three dimensional problems, the solution could be computationally expensive. Thanks to the use of periodic boundary condition in span-wise direction always employed in the simulations performed in this work, a solution method based on Fourier transform can be employed. Let N_1, N_2, N_3 be the number of grid points in the domain, the scalar ϕ can be written in Fourier series as:

$$\phi^{n+1}(i, j, k) = \sum_{m=0}^{N_3-1} \tilde{\phi}(i, j, m) \cos\left[\frac{\pi m}{N_3}\left(k - \frac{1}{2}\right)\right] \quad , \quad (2.30)$$

for $i = 1, 2, \dots, N_1$, $j = 1, 2, \dots, N_2$, $k = 1, 2, \dots, N_3$. Substituting (2.30) and the corresponding expansion for Q in (2.29), after some manipulation the following equation in the wave space is obtain:

$$\frac{\delta^2 \tilde{\phi}}{\delta x_1^2} + \frac{\delta^2 \tilde{\phi}}{\delta x_2^2} - k_m \tilde{\phi} = \tilde{Q}(i, j, m) \quad (2.31)$$

This particular algorithm leads to the solution of a series of two dimensional Helmholtz equations that can be quickly solved instead of solving large and sparse linear system. The solution for ϕ is then reconstruct applying (2.30).

2.4 Immersed Boundary Method

The immersed boundary method (IBM) designates the class of techniques where the calculation are performed over an eulerian grid that does not conform to the shape of the body in the flow, since the boundary conditions on the body surface are enforced adding to the Navier-Stokes equations appropriate forcing terms. Because of this key feature, the IBM are particularly suitable when dealing with moving and deforming bodies and allows to avoid complex grid generation and moving grids.

Peskin [8] presented the first application of this method to simulate the blood flow inside a heart with flexible valves. After him, several authors [1,2] have turned their attention to immersed boundary methods and the technique has become the principal tool to deal with fluid-structure interaction problems.

The method employed in the present work was proposed firstly by Pinelli et al. [9] and it is applicable to both cartesian and curvilinear grids.

2.4.1 Mathematical formulation

As introduced in section 1.3, the time advancement of the conservation equations is based on a fractional step method:

$$\frac{\hat{\mathbf{u}} - \mathbf{u}^n}{\Delta t} = -\mathcal{N}_l(\mathbf{u}^n, \mathbf{u}^{n-1}) - \mathcal{G}(\phi^n, \phi^{n-1}) + \frac{1}{Re}\mathcal{L}(\hat{\mathbf{u}}, \mathbf{u}^n) \quad , \quad (2.32)$$

$$\mathcal{L}\phi = \frac{1}{\Delta t}\mathcal{D}\hat{\mathbf{u}} \quad , \quad (2.33)$$

$$\frac{\mathbf{u}_i^{n+1} - \hat{\mathbf{u}}}{\Delta t} = -\mathcal{G}(\phi^{n+1}) \quad . \quad (2.34)$$

The sequence above is conveniently modified to imposed the desired boundary condition on the immersed body surface. The time advancement of the momentum equation is carried out in two stages. First, a prediction step analogous at (2.32) is performed, without any constraint on the embedded geometry:

$$\hat{\mathbf{u}} = \mathbf{u}^n - \Delta t[\mathcal{N}_l(\mathbf{u}^n, \mathbf{u}^{n-1}) - \mathcal{G}(\phi^n, \phi^{n-1}) + \frac{1}{Re}\mathcal{L}(\hat{\mathbf{u}}, \mathbf{u}^n)] \quad . \quad (2.35)$$

The velocity field obtained is then interpolated onto the embedded geometry Γ , which is discretized through a number of Lagrangian points with coordinate \mathbf{X}_k :

$$\hat{\mathbf{U}}(\mathbf{X}_k, t^n) = \mathcal{I}(\hat{\mathbf{u}}) \quad . \quad (2.36)$$

The values of $\hat{\mathbf{U}}(\mathbf{X}_k, t^n)$ are used to determine the distribution of singular forces along Γ that restore the desired boundary values $\mathbf{U}^\Gamma(\mathbf{X}_k, t^n)$ on Γ :

$$\hat{\mathbf{F}}(\mathbf{X}_k, t^n) = \frac{\mathbf{U}^\Gamma(\mathbf{X}_k, t^n) - \hat{\mathbf{U}}(\mathbf{X}_k, t^n)}{\Delta t} \quad . \quad (2.37)$$

The singular force field defined over Γ is then transformed by a convolution operator \mathcal{C} into a volume force field defined over the mesh points $\mathbf{x}_{i,j,k}$:

$$\hat{\mathbf{f}}(\mathbf{x}_{i,j,k}, t^n) = \mathcal{C}[\hat{\mathbf{F}}(\mathbf{X}_k, t^n)] \quad . \quad (2.38)$$

The force given by (2.38) is now used to solve again the momentum equation:

$$\hat{\mathbf{u}} = \mathbf{u}^n - \Delta t [\mathcal{N}_l(\mathbf{u}^n, \mathbf{u}^{n-1}) - \mathcal{G}(\phi^n, \phi^{n-1}) + \frac{1}{Re} \mathcal{L}(\hat{\mathbf{u}}, \mathbf{u}^n) + \hat{\mathbf{f}}] \quad . \quad (2.39)$$

Finally the algorithm completes the time step with the solution of the Poisson equation and the projection step.

The form of the interpolation and convolution operator is to be defined and it will be show in the next section.

2.4.2 Interpolation and Convolution

The interpolation and convolution operations are a key point of the immersed boundary method. The basic idea of the method is that, a given smooth function $f(s)$ at a certain point $x \in \Omega$ can be expressed as:

$$f(x) = \int_{\Omega} \delta(x - s) f(s) ds \quad , \quad (2.40)$$

where δ is the Dirac's delta.

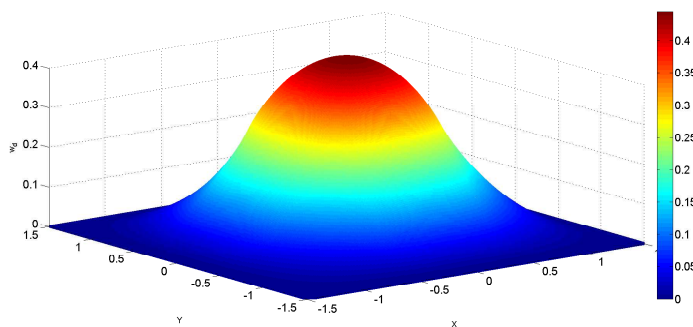


Figure 2.3: Kernel function proposed by Roma et al. [10] in two dimension. The dilatation parameter is taken equal to 1.

Numerically, the Dirac's delta is substituted by its discrete counterpart, called kernel function. The kernel function is characterized to be of compact support (it is non zero in the region Ω_I , called support, and zero outside it) and must respect some fundamentals properties of the analytical delta function. Many kernel function are available in the literature, in the present study the one proposed by Roma et al. [10] is employed, sketched in figure (2.3):

$$w_d = \begin{cases} \frac{1}{6}(5 - 3|r| - \sqrt{-3(1 - |r|)^2 - 1}), & \text{if } 0.5 < |r| < 1.5, \\ \frac{1}{3}(1 + \sqrt{-3r^2 + 1}) & \text{if } |r| < 0.5, \\ 0 & \text{otherwise,} \end{cases}$$

with $r = \frac{x-s}{d}$. The parameter d is called dilatation factor and defines the extension of the support. This function mimics the action of Diracs's delta and satisfy the following properties:

- $w_d(r - d)$ is continuous in $\forall r$;
- $w_d(r - d) = 0$, if $|r| \geq 1.5$;
- $\sum_l w_d(r - l) = 1, \forall l \in \mathbb{N}$;
- $\sum_l (r - l)w_d(r - l) = 0, \forall l, r$;
- $\sum_l [w_d(r - l)]^2 = \frac{1}{2}, \forall l, r$.

This guarantees the integral conservation of the force and its first moment during a spreading operation but can be met only on a uniform mesh.

Following Pinelli et al.[9] and Liu et al. [11], the kernel function is improved using a second order polynomial correction:

$$\tilde{w}_d = \sum_{i=0}^n b_i (x - s)^i w_d(x - s) \quad . \quad (2.41)$$

This step allows to use non uniform grids and makes the boundary of the immersed body sharper. The coefficients b_i can be found requiring to the modified window function to respect the reproducing conditions below:

$$\tilde{m}_i = \int_{\Omega_I} (x - s)^i \tilde{w}_d(x - s), \quad ds = \delta_{i0} \quad . \quad (2.42)$$

After some manipulations, a symmetric linear system is to be solved:

$$\begin{pmatrix} m_0 & m_1 & \dots & m_N \\ \dots & \dots & \dots & \dots \\ m_j & m_{j+1} & m & m_{N+j} \\ \dots & \dots & \dots & \dots \\ m_N & m_{N+1} & \dots & m_{2N} \end{pmatrix} \begin{pmatrix} b_0 \\ \vdots \\ b_j \\ \vdots \\ b_N \end{pmatrix} = \begin{pmatrix} 1 \\ \vdots \\ 0 \\ \vdots \\ 0 \end{pmatrix} \quad , \quad (2.43)$$

where m_j is given by:

$$m_j = \int_{\Omega_I} (x - s)^j w_d(x - s) ds \quad . \quad (2.44)$$

In three dimensions the window function w_d can be given as a cartesian product of w_d with itself:

$$w_{\delta,\eta,\sigma} = w_\delta(x - s)w_\eta(y - t)w_\sigma(z - v). \quad (2.45)$$

Here δ, η, σ are the dilatation factors in the three coordinate directions. As mentioned before, the window function is corrected assuming the following form:

$$\begin{aligned} \tilde{w}_d(x - s, t - y, t, z - v) = & [b_0 + (x - s)b_1 + (y - t)b_2 + (z - v)b_3 \\ & + b_4(x - s)(y - t) + (y - t)(z - v)b_5 + (z - v)(x - s)b_6 \\ & + (x - s)^2 b_7 + (y - t)^2 b_8 + (z - v)^2 b_9] w_d(x - s, ty, t, z - v). \end{aligned} \quad (2.46)$$

The coefficients b_i can be found solving the linear system (2.42).

The matrix M , called moment matrix, for three-dimensional problems reads :

$$M = \begin{pmatrix} m_{0,0,0} & m_{1,0,0} & m_{0,1,0} & m_{0,0,1} & m_{1,1,0} & m_{0,1,1} & m_{1,0,1} & m_{2,0,0} & m_{0,2,0} & m_{0,0,2} \\ m_{1,0,0} & m_{2,0,0} & m_{1,1,0} & m_{1,0,1} & m_{2,1,0} & m_{1,1,1} & m_{2,0,1} & m_{3,0,0} & m_{1,2,0} & m_{1,0,2} \\ m_{0,1,0} & m_{1,1,0} & m_{0,2,0} & m_{0,1,1} & m_{1,2,0} & m_{0,2,1} & m_{1,1,1} & m_{2,1,0} & m_{0,3,0} & m_{0,1,2} \\ m_{0,0,1} & m_{1,0,1} & m_{0,1,1} & m_{0,0,2} & m_{1,1,1} & m_{0,1,2} & m_{1,0,2} & m_{2,0,1} & m_{0,2,1} & m_{0,0,3} \\ m_{1,1,0} & m_{2,1,0} & m_{1,2,0} & m_{1,1,1} & m_{2,2,0} & m_{1,2,1} & m_{2,1,1} & m_{3,1,0} & m_{1,3,0} & m_{1,1,2} \\ m_{0,1,1} & m_{1,1,1} & m_{0,2,1} & m_{0,1,2} & m_{1,2,0} & m_{0,2,2} & m_{1,1,2} & m_{2,1,1} & m_{0,3,1} & m_{0,1,3} \\ m_{1,0,1} & m_{2,0,1} & m_{1,1,1} & m_{1,0,2} & m_{2,1,1} & m_{1,1,2} & m_{2,0,2} & m_{3,0,1} & m_{1,2,1} & m_{1,0,3} \\ m_{2,0,0} & m_{3,0,0} & m_{2,1,0} & m_{2,0,1} & m_{3,1,0} & m_{2,1,1} & m_{3,0,1} & m_{4,0,0} & m_{2,2,0} & m_{2,0,2} \\ m_{0,2,0} & m_{1,2,0} & m_{0,3,0} & m_{0,2,1} & m_{1,3,0} & m_{0,3,1} & m_{1,2,1} & m_{2,2,0} & m_{0,4,0} & m_{0,2,2} \\ m_{0,0,2} & m_{1,0,2} & m_{0,1,2} & m_{0,0,3} & m_{1,1,2} & m_{0,1,3} & m_{1,0,3} & m_{2,0,2} & m_{0,2,2} & m_{0,0,4} \end{pmatrix}.$$

with $m_{i,j,k} = \int_{\Omega_I} (x-s)^i (y-t)^j (z-v)^k \tilde{w}_d(x-s, t-y, z-v) ds dt dv$.

2.4.3 Numerical Implementation

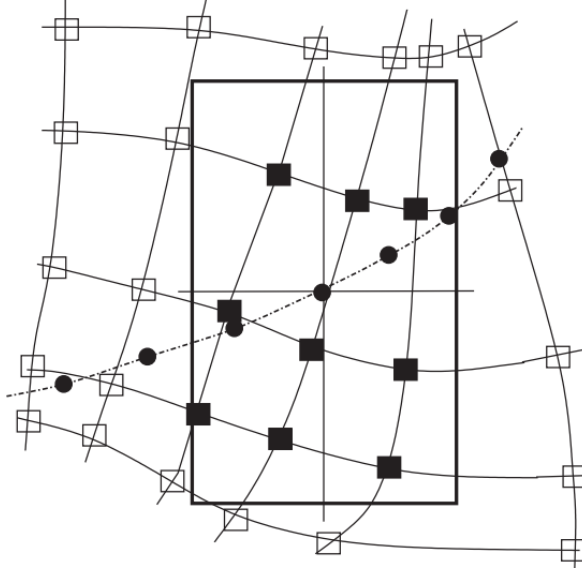


Figure 2.4: Definition of the support cage in two dimension. The dashed line is the embedded curve and the solid line is the rectangular support cage Ω_I . \bullet Lagrangian markers on the embedded curve, \square grid points, \blacksquare grid points within the support.

The first step is to discretize the embedded geometry into a number of nodes $\mathbf{X}_i, i = 1, \dots, N_e$. Around each node \mathbf{X}_I a cubic/rectangular cage Ω_I is defined that contains at least three nodes of underlying mesh in each direction (9 in 2D and 27 in 3D) and that will be the support for the window function (2.45). The cage and the underlying mesh are sketched in figure 2.4. The edges of the cage measure $3\delta, 3\eta, 3\sigma$ in x, y, z direction respectively, where δ, η, σ are the dilatations factors.

To determine of support centred in \mathbf{X}_I , the closest node to \mathbf{X}_I , $\mathbf{x}_{\hat{i}, \hat{j}, \hat{k}}$, is found and the distance $\Delta \mathbf{x} = |\mathbf{X}_I - \mathbf{x}_{\hat{i}, \hat{j}, \hat{k}}|$ is calculated; then a set of nodes neighbouring $\mathbf{x}_{\hat{i}, \hat{j}, \hat{k}}$, $\mathcal{N}_I = \mathbf{x}_{\hat{i}+l, \hat{j}+m, \hat{k}+n}, l, m, n = -1, 0, 1$ is considered and the following quantities

are evaluated:

$$\begin{cases} h_x^+(\mathbf{X}_I) = \max(|x_{i,j,k} - x_{i-1,j,k}| : x_{i,j,k}, x_{i-1,j,k} \in \mathcal{N}_I), \\ h_x^-(\mathbf{X}_I) = \min(|x_{i,j,k} - x_{i-1,j,k}| : x_{i,j,k}, x_{i-1,j,k} \in \mathcal{N}_I), \\ h_y^+(\mathbf{X}_I) = \max(|y_{i,j,k} - y_{i,j-1,k}| : y_{i,j,k}, y_{i,j-1,k} \in \mathcal{N}_I), \\ h_y^-(\mathbf{X}_I) = \min(|y_{i,j,k} - y_{i,j-1,k}| : y_{i,j,k}, y_{i,j-1,k} \in \mathcal{N}_I), \\ h_z^+(\mathbf{X}_I) = \max(|z_{i,j,k} - z_{i,j,k-1}| : z_{i,j,k}, z_{i,j,k-1} \in \mathcal{N}_I), \\ h_z^-(\mathbf{X}_I) = \min(|z_{i,j,k} - z_{i,j,k-1}| : z_{i,j,k}, z_{i,j,k-1} \in \mathcal{N}_I). \end{cases} \quad (2.47)$$

Based on these values, the length of the edges of the cube through the local dilatation factor are:

$$\delta_I = \left(\frac{5}{6}h_x^+(\mathbf{X}_I) + \frac{1}{6}h_x^-(\mathbf{X}_I) + \frac{1}{9}\Delta x\right) \quad , \quad (2.48)$$

$$\eta_I = \left(\frac{5}{6}h_y^+(\mathbf{X}_I) + \frac{1}{6}h_y^-(\mathbf{X}_I) + \frac{1}{9}\Delta y\right) \quad , \quad (2.49)$$

$$\sigma_I = \left(\frac{5}{6}h_z^+(\mathbf{X}_I) + \frac{1}{6}h_z^-(\mathbf{X}_I) + \frac{1}{9}\Delta z\right) \quad . \quad (2.50)$$

The set of grid nodes that fall within the cage is sought:

$$\mathcal{S}_I = \left\{ \mathbf{x}_{i,j,k} : |x_{i,\hat{j},\hat{k}} - x_{i,j,k}| < \frac{3}{2}\delta_I, |y_{i,\hat{j},\hat{k}} - y_{i,j,k}| < \frac{3}{2}\eta_I, |z_{i,\hat{j},\hat{k}} - z_{i,j,k}| < \frac{3}{2}\sigma_I \right\} \quad (2.51)$$

the small fraction $\frac{1}{9}\Delta\mathbf{x}$ is added to avoid the support boundary touching some of support nodes; In this case the window function would be zero at those node, making the matrix \mathbf{M} , previously defined, singular.

The elements of the moment matrix are numerically evaluated using, for example, the mid-point rule:

$$m_{i,j,k} = \sum_{l,h,n \in \mathcal{S}_I} (x_{l,h,n} - X_I)^i (y_{l,h,n} - Y_I)^j (z_{l,h,n} - Z_I)^k w_{\delta_I, \eta_I, \sigma_I} \Delta V_{l,h,n} \quad , \quad (2.52)$$

where $\Delta V_{l,h,n}$ is the volume of the cell centred in $\mathbf{x}_{l,h,n}$. The methodology developed allow the definition of the modified window function to be used in the convolution integral in interpolation and spreading operations. In particular, given a component of the velocity field $u_i(x, y, z)$ known at a grid node $\mathbf{x}_{l,h,n} \in \mathcal{S}_I$, the interpolated value at node \mathbf{X}_I can be approximated by:

$$U_i(\mathbf{X}_I) = \mathcal{I}(u_i) = \sum_{l,h,n \in \mathcal{S}_I} u_i(\mathbf{x}_{l,h,n}) \tilde{w}_{\delta_I, \eta_I, \sigma_I} \Delta V_{l,h,n} \quad . \quad (2.53)$$

Once the force component $F_i(\mathbf{X}_I)$ is found from (2.37), the distribution of singular forces over the mesh nodes can be obtained using the following convolution operator:

$$f_i(\mathbf{x}_{l,h,n}) = \mathcal{C}(F_i) = \sum_{I=1}^{N_e} F_i(\mathbf{X}_I) \tilde{w}_{\delta_I, \eta_I, \sigma_I} \epsilon_I \Delta S_I \quad , \quad (2.54)$$

where Δs_I is the length of the arch joining $X_{I+\frac{1}{2}}$ to $X_{I-\frac{1}{2}}$ and ϵ_I is a characteristic strip-width. To determinate the correct value of ϵ_I the value of the force in the point \mathbf{X}_I obtained by interpolation of the nodes of the underlying grid is considered:

$$F_i(\mathbf{X}_I) = \sum_{l,h,n \in S_I} f_i(\mathbf{x}_{l,h,n}) \tilde{w}_{\delta_I, \eta_I, \sigma_I} \Delta V_{l,h,n} \quad . \quad (2.55)$$

By replacing the values of f_i with those that would be obtained for the discrete spreading operation (2.54), the following condition is obtained:

$$F_i(\mathbf{X}_I) = \sum_{K=1}^{N_e} a_{I,K} \epsilon_K F_i(\mathbf{X}_K) \quad , i = 1, \dots, N_e \quad , \quad (2.56)$$

where $a_{I,K}$ is the discrete integral product of the I^{th} and the K^{th} window functions over the support of the former one multiplied by the node spacing ΔS_K between the two nodes:

$$a_{I,K} = \Delta S_K \sum_{l,h,n \in S_I} \tilde{w}_{\delta_I, \eta_I, \sigma_I}(\mathbf{x}_{l,h,k} - \mathbf{X}_I) \tilde{w}_{\delta_I, \eta_I, \sigma_I}(\mathbf{x}_{l,h,k} - \mathbf{X}_K) \Delta V_{l,h,n} \quad . \quad (2.57)$$

In matrix notation, and imposing that the local width ϵ is independent of the actual force distribution F_i , the linear system (2.56) can be written as:

$$A \vec{\epsilon} = \vec{1} \quad . \quad (2.58)$$

The conditioning of the matrix A depends on the ratio between the node spacing δs_K and the eulerial grid size. This lead to choose a number of nodes to discretize the immersed body such that the above ratio is near one.

2.5 Filament Governing Equations

The filament model is crucial in order to obtain physical results from the simulations. In the present study the filament is assumed to be:

- flexible: the filament can bend in the space and reacts to a flexural force generating a restoring force.
- inextensible: the filament length remains constant during its motion even if a system of external forces is acting on it.
- massive: the filament has its own material density ρ_s different, in general, from the surrounding fluid density ρ_f .

A curvilinear coordinate s is used to specify the position along the filament. The governing equation for a filament, written in a Lagrangian form, is:

$$\Delta\rho\frac{\partial^2\mathbf{X}}{\partial t^2} = \frac{\partial}{\partial s}\left(T\frac{\partial\mathbf{X}}{\partial s}\right) - K_B\frac{\partial^4\mathbf{X}}{\partial s^4} + \Delta\rho\mathbf{g} - \mathbf{F} \quad , \quad (2.59)$$

where s is the arclength, $\Delta\rho$ denotes the density difference between the filament and the surrounding fluid, $\mathbf{X}(s, t) = (X(s, t), Y(s, t), Z(s, t))^T$ is the filament position, T is the tension along the filament, K_B is the bending rigidity, \mathbf{g} is the gravity acceleration and $\mathbf{F}(s, t) = (F_x(s, t), F_y(s, t), F_z(s, t))^T$ is the Lagrangian force exerted on the filament by surrounding fluid. In the equation (2.59) there are four unknowns (position vector $\mathbf{X}(s, t)$ and the tension $T(s, t)$) and another equation is needed to close the problem.

The inextensibility condition is the constrain that leads to the following closure equation:

$$\frac{\partial\mathbf{X}}{\partial s} \cdot \frac{\partial\mathbf{X}}{\partial s} = 1 \quad . \quad (2.60)$$

The boundary conditions must be specified at the free end ($s = L$) and at the fixed end ($s = 0$) of the filament. At the free end we have that:

$$T(L, t) = 0, \quad \frac{\partial^2\mathbf{X}(L, t)}{\partial s^2} = \mathbf{0} \quad . \quad (2.61)$$

At the fixed end two different types of boundary condition may be chosen. The first one is the simply supported condition:

$$\mathbf{X}(0, t) = \mathbf{X}_0, \quad \frac{\partial^2\mathbf{X}(0, t)}{\partial s^2} = \mathbf{0} \quad , \quad (2.62)$$

and the other one is the clamped condition

$$\mathbf{X}(0, t) = \mathbf{X}_0, \quad \frac{\partial\mathbf{X}(0, t)}{\partial s} = \boldsymbol{\alpha} \quad . \quad (2.63)$$

Using the clamped condition, it is possible to impose the filament slope at the fixed end. This condition will be employed for the calculation later.

2.5.1 Non-dimensionalization of the Equations

The equations (2.59) and (2.60) can be non-dimensionalized by introducing and applying the following characteristic scales:

- A characteristic length L_c of the problem for the position \mathbf{X} and the arclength s . L_c is assumed to be the filament length if the filament is standing alone in a uniform flow. Otherwise, if the filament is placed behind a circular cylinder, the cylinder diameter D is taken as characteristic length.
- The far-field velocity U_∞ for the velocity.
- U_∞/L_c for time.
- $\Delta\rho U_\infty^2/L_c$ for the lagrangian force acting on the filament.

This yields non-dimensional quantities denoted by asterisk, i.e:

$$\mathbf{X}^* = \mathbf{X}/L_c \quad (2.64)$$

$$t^* = U_\infty t/L_c \quad (2.65)$$

$$\mathbf{F}^* = \mathbf{F}L_c/\Delta\rho U_\infty^2 \quad (2.66)$$

Scaling (2.59) and (2.60) with relations (2.6)-(2.8), the non-dimensionalized equations are:

$$\frac{\partial^2 \mathbf{X}^*}{\partial t^{*2}} = \frac{\partial}{\partial s^*} (T^* \frac{\partial \mathbf{X}^*}{\partial s^*}) - K_B^* \frac{\partial^4 \mathbf{X}^*}{\partial s^{*4}} + Ri \frac{\mathbf{g}}{|g|} - \mathbf{F}^* \quad (2.67)$$

From now on when using this equations the asterisks will be omitted.

2.6 Discretisation of the Filament Equation

2.6.1 Time And Space Discretisation

Because of its complexity, an analytical solution is available for the set of equations (2.59) and (2.60) under the hypothesis that $K_B = 0$ and only if the filament is subjected to a small amplitude motion [12]. These assumptions are often too restrictive and, in order to recreate a more physical results of the filament motion, a computational approach have to be used. In the next section will be presented the numerical method employed to solve the filament problem. 2.5.

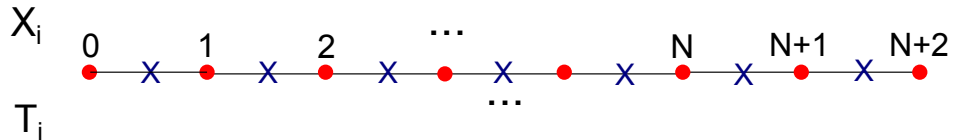


Figure 2.5: Variable arrangement for a flexible filament. The red \bullet is the Lagrangian node, while the blue x is tension node.

Following Huang et al.'s formulation [12], the discretisation of the filament governing equations is performed in a staggered arrangement, as shown in figure 2.5. The filament

is discretized with a finite number of Lagrangian nodes \mathbf{X}_i ; tension nodes T_i are placed between the coordinate markers. The nodes $i = -1, N + 1, N + 2$ are ghost nodes and they are used only to impose the boundary conditions.

The time and space discretized set of equations to be solved reads:

$$\frac{\mathbf{X}^{n+1} - 2\mathbf{X}^n + \mathbf{X}^{n-1}}{\Delta t^2} = D_s(T^{n+1}D_s\mathbf{X}^{n+1}) - K_B D_{ssss}\mathbf{X}^{n+1} + Ri \frac{\mathbf{g}}{|g|} + \mathbf{F}^n \quad , \quad (2.68)$$

$$D_s\mathbf{X}^{n+1} \cdot D_s\mathbf{X}^{n+1} = 1 \quad , \quad (2.69)$$

where D_s and D_{ssss} are the discrete counterpart of first and fourth order derivatives respect to the parametric coordinate s . The tension and the bending term in (2.68) are discretized as follow for nodes $i \in [2, N - 2]$:

$$\begin{cases} D_s(TD_s\mathbf{X}) = \frac{T_i(\mathbf{X}_{i+1} - \mathbf{X}_i) - T_{i-1}(\mathbf{X}_i - \mathbf{X}_{i-1})}{\Delta s^2} \\ K_B D_{ssss}\mathbf{X} = K_B \frac{\mathbf{X}_{i-2} - 4\mathbf{X}_{i-1} + 6\mathbf{X}_i - 4\mathbf{X}_{i+1} + \mathbf{X}_{i+2}}{\Delta s^4} \\ D_s\mathbf{X} \cdot D_s\mathbf{X} = \frac{(\mathbf{X}_{i+1} - \mathbf{X}_i) \cdot (\mathbf{X}_{i+1} - \mathbf{X}_i)}{\Delta s^2} \end{cases} \quad (2.70)$$

Substituting relations (2.70) and algebraically rearranging the terms, it is possible to find a suitable form for equation (2.68):

$$-\alpha \mathbf{X}_{i-2}^{n+1} + (T_j^{n+1} + 4\alpha) \mathbf{X}_{i-1}^{n+1} - [\beta + T_{i+1}^{n+1} + T_i^{n+1} + 6\alpha] \mathbf{X}_i^{n+1} + (T_{i+1}^{n+1} + 4\alpha) \mathbf{X}_{i+1}^{n+1} - \alpha \mathbf{X}_{i+2}^{n+1} + \mathbf{X}^* = 0 \quad , \quad (2.71)$$

with:

- $\alpha = \frac{K_B}{\Delta s^2}$,
- $\beta = \frac{\Delta s^2}{\Delta t}$,
- $\mathbf{X}^* = 2\mathbf{X}^n - \mathbf{X}^{n-1}$.

The equations for the nodes $i = 1, N - 1, N$ can be found applying the correct boundary conditions at the fixed and at the free end of the filament.

2.7 Boundary Conditions

2.7.1 Fixed end

At the fixed end $s = 0$, the filament equation can be conveniently rearranged. Assuming $D_{ssss}\mathbf{X} = 0$, multiplying by $D_s\mathbf{X}$ both sides of the equation and remembering boundary condition (2.62), equation (2.59) reduces to:

$$\frac{\partial T}{\partial s} + T \frac{\partial^2 \mathbf{X}}{\partial s^2} \cdot \frac{\partial \mathbf{X}}{\partial s} + (Ri \frac{\mathbf{g}}{g} + \mathbf{F}) \cdot \frac{\partial \mathbf{X}}{\partial s} = 0 \quad , \quad (2.72)$$

or, in its discrete counterpart:

$$D_s T^{n+1} + T^{n+1} D_s D_s \mathbf{X}^{n+1} \cdot D_s \mathbf{X}^{n+1} + (Ri \frac{\mathbf{g}}{g} + \mathbf{F}^n) \cdot D_s \mathbf{X}^{n+1} = 0 \quad . \quad (2.73)$$

Equation (2.72) can be discretized in the same manner employed for equation (2.59) and it reduces to:

$$\begin{aligned} \frac{T_1^{n+1} - T_0^{n+1}}{\Delta s} + (T_1 + T_0) \left(\frac{\mathbf{X}_{-1}^{n+1} - 2\mathbf{X}_0^{n+1} + \mathbf{X}_1^{n+1}}{\Delta s^2} \right) \cdot \frac{(\mathbf{X}_1^{n+1} - \mathbf{X}_{-1}^{n+1})}{2\Delta s} + \\ + \left(\mathbf{F}^n + Ri \frac{\mathbf{g}}{g} \right) \cdot \frac{(\mathbf{X}_1^{n+1} - \mathbf{X}_{-1}^{n+1})}{2\Delta s} . \end{aligned} \quad (2.74)$$

The value of position at the ghost point \mathbf{X}_{-1} can be easily found from the boundary conditions as follow:

$$\begin{cases} \mathbf{X}_{-1}^{n+1} - 2\mathbf{X}_0^{n+1} + \mathbf{X}_1^{n+1} = 0 & , \text{ for the simply supported filament.} \\ \mathbf{X}_1^{n+1} - \mathbf{X}_{-1}^{n+1} = 2\Delta s \boldsymbol{\alpha} & , \text{ for the clamped filament.} \\ \mathbf{X}_{s=0}^{n+1} = \mathbf{X}_0^{n+1} . \end{cases} \quad (2.75)$$

Substituting the value for \mathbf{X}_{-1}^{n+1} in equation (2.74), the final form of the filament equation at the fixed end for the simply supported boundary condition can be written as:

$$T_1^{n+1} - T_0^{n+1} + \left(\mathbf{F}^n + Ri \frac{\mathbf{g}}{g} \right) \cdot (\mathbf{X}_1^{n+1} - \mathbf{X}_0) = 0 \quad , \quad (2.76)$$

and for the clamped boundary conditions:

$$\begin{aligned} \Delta s (T_1^{n+1} - T_0^{n+1}) + (T_1 + T_0) \left(\frac{\mathbf{X}_1^{n+1} - \mathbf{X}_0^{n+1} - 2\Delta s \boldsymbol{\alpha}}{\Delta s^2} \right) \cdot \boldsymbol{\alpha} \\ + \left(\mathbf{F}^n + Ri \frac{\mathbf{g}}{g} \right) \cdot \boldsymbol{\alpha} \Delta s . \end{aligned} \quad (2.77)$$

2.7.2 Free end

At the free end ($s = L$), boundary conditions (2.61) translates in:

$$\begin{cases} \mathbf{X}_{N-1}^{n+1} - 2\mathbf{X}_N^{n+1} + \mathbf{X}_{N+1}^{n+1} = 0 \\ \mathbf{X}_N^{n+1} - 2\mathbf{X}_{N+1}^{n+1} + \mathbf{X}_{N+2}^{n+1} = 0 \Rightarrow \mathbf{X}_{N+2} - 3\mathbf{X}_N + 2\mathbf{X}_{N-1} = 0 \\ T_{N+1}^{n+1} = -T_N^{n+1} . \end{cases} \quad (2.78)$$

Substituting the values for \mathbf{X}_{N+1}^{n+1} and \mathbf{X}_{N+2}^{n+1} in equation (2.68), the equations for node $i = N - 1$ result

$$\begin{aligned} -\alpha \mathbf{X}_{N-3}^{n+1} + (T_i^{n+1} + 4\alpha) \mathbf{X}_{N-2} - [\beta + T_{i+1}^{n+1} + T_i^{n+1} + 5\alpha] \mathbf{X}_{N-1} + \\ (T_{i+1}^{n+1} + 2\alpha) \mathbf{X}_N^{n+1} + \mathbf{X}^* = 0 \quad , \end{aligned} \quad (2.79)$$

while for node $i = N$ it is:

$$-\alpha \mathbf{X}_{N-2}^{n+1} + (2T_i^{n+1} + 2\alpha) \mathbf{X}_{N-1}^{n+1} - [\beta + \alpha + 2T_i^{n+1}] \mathbf{X}_N^{n+1} + \mathbf{X}^* = 0 \quad . \quad (2.80)$$

It is worth to note that the free end of the filament does not correspond to a tension point. Thus, in order to obtain discrete boundary condition for $T(L, t)$, a linear distribution of tension is hypothesized between N and $N + 1$.

2.8 Numerical Resolution of Filament's Equation

The relations (2.70), (2.72),(2.79) and (2.80) represent a set of $4N + 1$ non-linear equations in the unknowns $T_0, T_i, \mathbf{X}_i^{n+1}$. The system can be conveniently put in the following form:

$$\begin{cases} F_1(\mathbf{X}_1^{n+1}, T_1^{n+1}, T_0^{n+1}) = 0 \\ F_2(\mathbf{X}_2^{n+1}, T_1^{n+1}) = 0 \\ \vdots \\ F_i(\mathbf{X}_i^{n+1}, T_i^{n+1}) = 0 \\ \vdots \\ F_{4N+1}(\mathbf{X}_N^{n+1}, T_N^{n+1}) = 0 \end{cases} \quad (2.81)$$

where F_i represent the i -th equation for the i -th lagrangian node.

Because of non linearity, the iterative Newton-Raphson method has been employed in order to solve the system (2.81). It consists in solving, at each time step, the following linearized system k times until convergence:

$$\begin{cases} \mathbf{J}(u^{(k)})\delta\mathbf{u}^{(k)} = -\mathbf{F}^k(\mathbf{u}^{(k)}) \\ \delta\mathbf{u}^{(k+1)} = \mathbf{u}^{(k+1)} - \mathbf{u}^{(k)} \end{cases} \quad (2.82)$$

where:

- \mathbf{u} is the vector containing the unknowns:

$$\mathbf{u} = (T_0, T_1, x_1, y_1, z_1, T_2, x_2, y_2, z_2, \dots, T_N, x_N, y_N, z_N)^T$$

- \mathbf{J} is the Jacobian matrix containing the derivatives of equations (2.81) with respect to the unknowns u_i :

$$\mathbf{J} = \begin{bmatrix} \frac{\partial F_1^{(k)}}{\partial u_1} & \frac{\partial F_1^{(k)}}{\partial u_2} & \cdots & \frac{\partial F_1^{(k)}}{\partial u_N} \\ \frac{\partial F_2^{(k)}}{\partial u_1} & \frac{\partial F_2^{(k)}}{\partial u_2} & \cdots & \frac{\partial F_2^{(k)}}{\partial u_N} \\ \vdots & \vdots & \ddots & \vdots \\ \frac{\partial F_N^{(k)}}{\partial u_1} & \frac{\partial F_N^{(k)}}{\partial u_2} & \cdots & \frac{\partial F_N^{(k)}}{\partial u_N} \end{bmatrix}$$

- \mathbf{F}^k is the vector containing the residual of equations (2.81) at the k-th iteration.

The superscript $\bullet^{(n+1)}$ is omitted for clarity. Convergence is considered to be reached if the maximum residual of equations (2.81) is less than 10^{-10} . The filament model is implemented insied a Navier-Stoked solver and it is used to update the position of the object during the simulations.

Chapter 3

Validation

This chapter is dedicated to the validation of the code and comparisons with previous works will be presented. In particular the following test cases will be proposed, with the aim of testing the code in all of its part and in different situations:

- Pure gravity driven filament: the filament is dropped from an initial angle and it falls under the action of gravity force. This numerical experiment is important in order to test the accuracy of the routine dedicated to the solution of the filament equation, that follows the procedure developed in section 2.6.
- Single filament in a uniform flow: a single filament stands in a channel and it is subjected to a uniform flow that forces the filament to flap. The simulation reproduces the experiments conducted by Zhang et al. [1] and the results are compared with the numerical calculations performed by Huang et al. [12] and Favier et al. [13].
- Single filament behind a two dimensional circular cylinder: a single filament is free to flap behind a two dimensional circular cylinder, forced by the unsteady wake generated by the bluff body. The results are compared with Bagheri et al. [3].

The governing differential equations are discretized on a collocated grid using a finite-volume code. The method of Rhie and Chow is used to avoid pressure oscillations. Both convective and diffusive fluxes are approximated by second-order central differences. A second-order-accurate semi-implicit fractional-step procedure is used for the temporal discretization. The Crank-Nicolson scheme is used for the wall-normal diffusive terms, and the Adam-Brashforth scheme for all the others terms. The code has been equipped with the immersed boundary method explained in section 1.5 and the filament position is computed using the model in section 1.8.

3.1 Validation Of The Filament Model

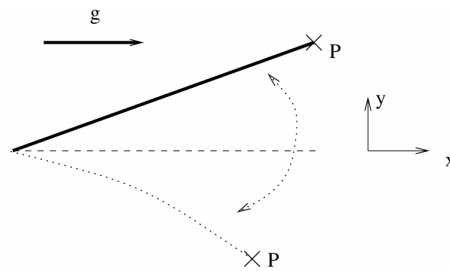


Figure 3.1: Initial position of the filament falling under gravity.

The filament numerical model presented in section 2.6 is validated against Huang et al. [12]. The filament is subjected to only gravity force, acting in x -direction as shown in figure 3.1, and it is free to fall and to oscillate. The test cases involves the use of the following setup:

Pure gravity driven filament		
Length	L	1.0
Bending Stiffness	K_b	0.01
Richardson number	Ri	10
Initial angle	θ	18
N of Lagrangian points	N	64

Table 3.1: parameters used in the test case 1 for the filament

Parameters test 2		
Length	L	1.0
Bending Stiffness	K_b	0.0
Richardson number	Ri	10
Initial angle	θ	2
N of Lagrangian points	N	64

Table 3.2: parameters used in the test case 2 for the filament.

In figure 3.2(a)-3.3(b) is sketched the path of the free extremity of the filament (point P in figure 3.1) normalized with the filament length, whereas in figure 3.2(b)-3.3(b) is drawn the filament motion between 0 and 0.8 time unit.

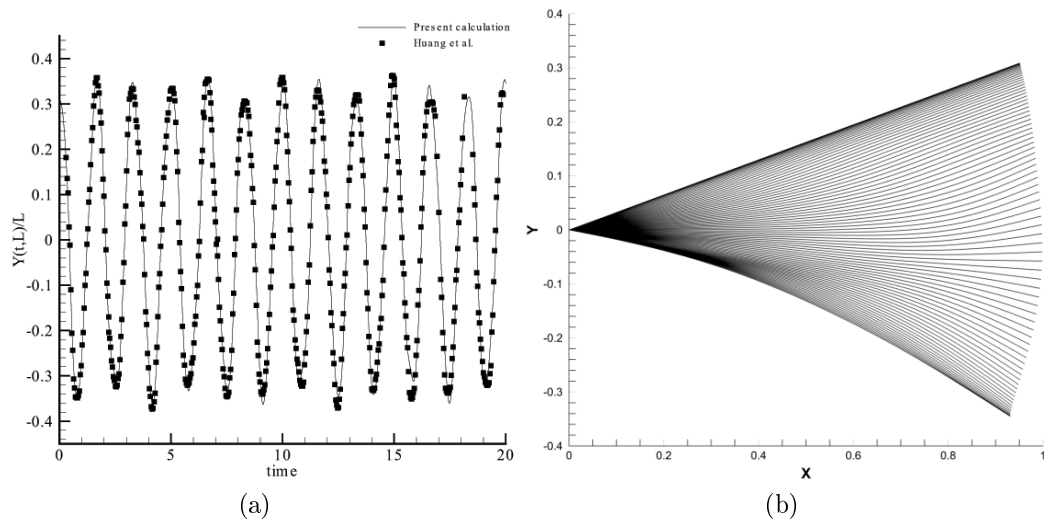


Figure 3.2: Pure gravity driven filament for the case with stiffer filament. (a) time evolution of the free extremity and validation against Huang et al. (b) Superposition of the filament positions between 0 and 0.8 time unit.

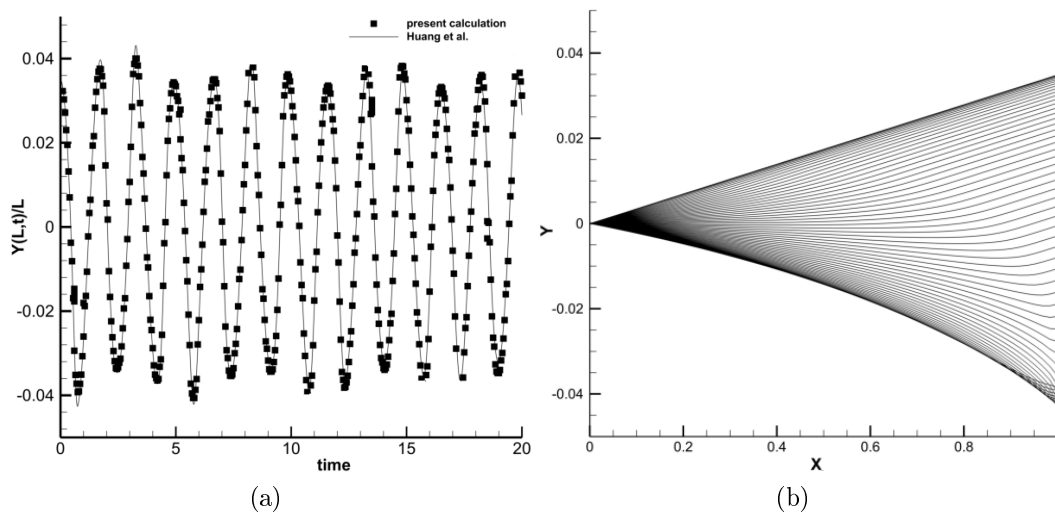


Figure 3.3: Pure gravity driven filament with zero bending coefficients. (a) time evolution of the free extremity end and validation against Huang et al. (b) Superposition of the filament positions between 0 and 0.8 time unit.

The comparisons shown a very good agreement respect to the literature. The filaments bends under the action of the gravity force and start pendulum-like motion whose amplitude is influenced by the bending coefficients and the initial angle, as expected.

3.2 Single Filament in a Uniform Flow

In the present section the numerical experiment of a single filament flapping in an incoming uniform flow will be reproduced. The results will be compared with the calculation performed by Huang et al. [?] and Favier et al. [13].

A sketch of the setup is shown in figure 3.4.

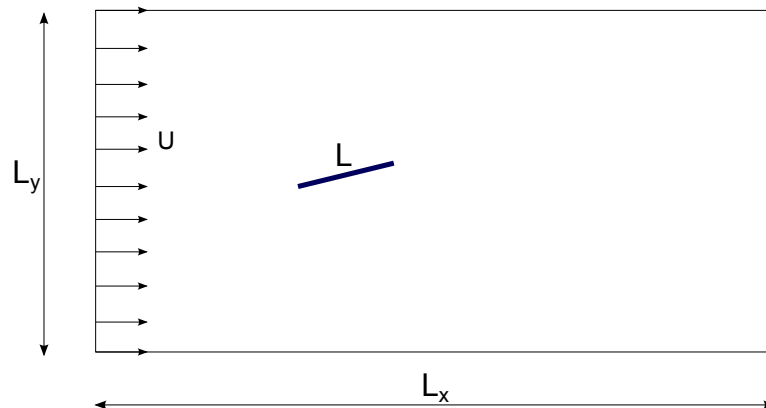


Figure 3.4: Sketch of the setup for a single filament immersed in a uniform flow.

The filament is standing alone in a channel and it is free to flap under the force exerted by the fluid over the body. The simulation setup parameters are summarized in table 3.3.

Filament in a uniform flow		
Length	L	1.0
filament density	ρ_s	1.5
Bending Stiffness	K_b	10^{-3}
Reynolds number	$\frac{UL}{\nu}$	200
Richardson number	Ri	0.5
Initial angle	θ	18
N of Lagrangian points	N	64

Table 3.3: Parameter used in the present simulation.

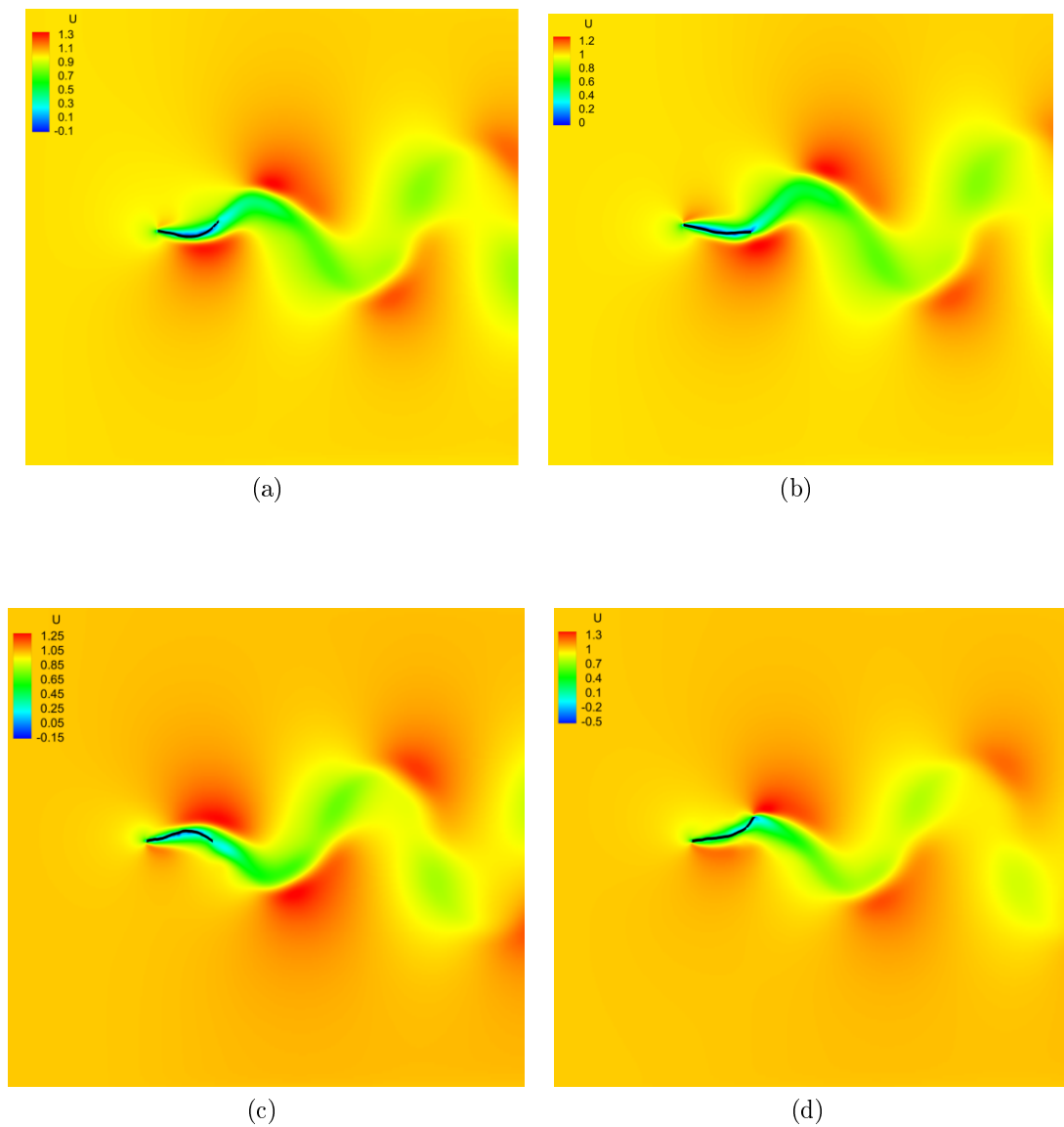
Free slip boundary condition at the top and bottom of the domain are chosen and the simply supported condition at the fixed end of the filament is imposed according to the reference cases. The Navier-Stokes equation are solved using a fractional step finite volume method together with the immersed boundary method presented in section 1.5, used to simulate the presence of the filament.

The grid used is a simple cartesian grid with uniform spacing in x and y direction. The computational domain has the following characteristics, presented in table 3.4:

Domain setup		
x-length	L_x	4
y-length	L_y	4
Grid size	256X128	

Table 3.4: Computational domain setup.

The filament is forced by the fluid and it is induced to flap up and down reaching a maximum excursion. The flap amplitude is limited by the combined action of the fluid itself and of the bending and tension forces that operate to straighten the filament: the result is a self-sustained, symmetric flapping cycle. In figure 3.5 is shown the filament during its motion and the computed flow field.

Figure 3.5: Snapshots of u -velocity field during the motion of the filament.

The free end of the filament, shown in figure 3.6 (a), is compared with the results obtained by Huang et al. [12] and by Favier et al. [13]. In figure 3.6(b) is also shown a qualitative comparison of the flapping cycle with the experiments conducted by Zhang et al. [1].

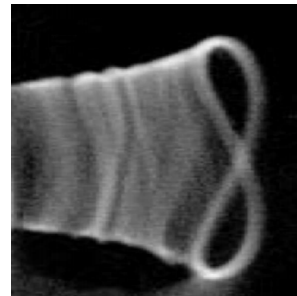
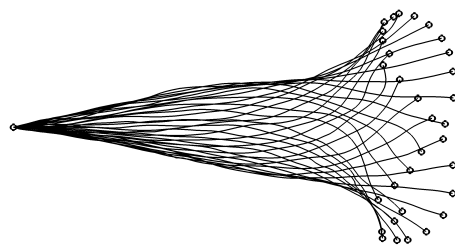
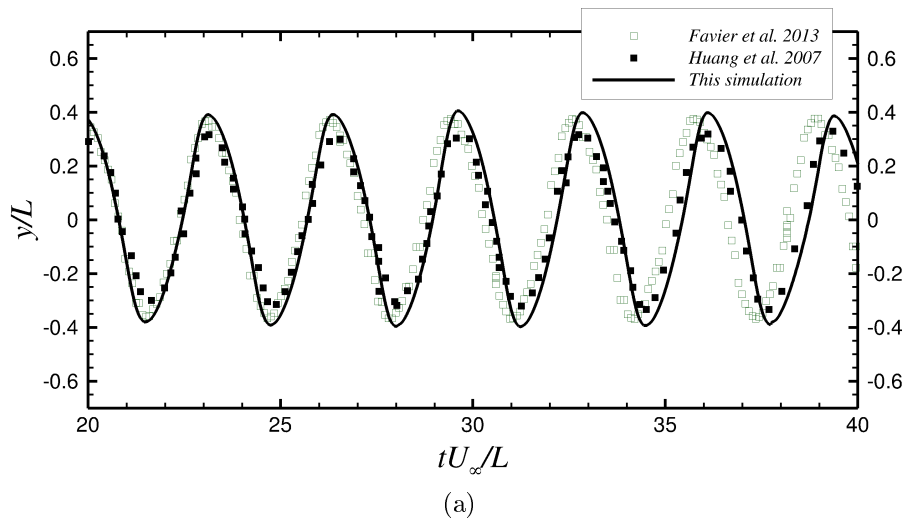


Figure 3.6: Flapping filament in a uniform flow. (a) time history of the free end of the filament.(b) flapping cycle computed in the present simulation. (c) Flapping cycle from the experiments by Zhang et al.

The simulation shows a good agreement with the validation cases: the filament exhibits the characteristic *figure-eight* orbit and the free extremity time evolution has a good match with previous works.

3.3 Hinged Filament behind a 2D Circular Cylinder

This section is dedicated to the last validation cases proposed. A flexible filament is hinged behind a two dimensional circular cylinder and it is free to flap in the wake generated by the bluff body. The initial position of the filament is symmetric with respect to the wall normal direction and the object is subject to an unperturbed incoming flow. A sketch of the setup is shown in figure 3.7:

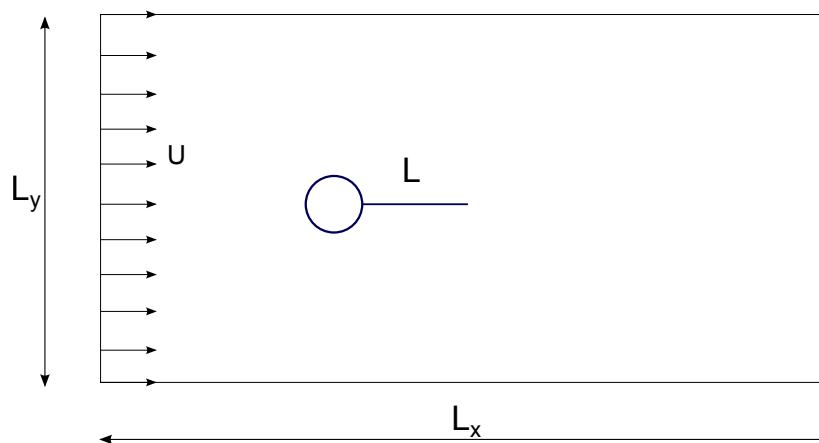


Figure 3.7: Sketch of the setup for the filament hinged behind a cylinder .

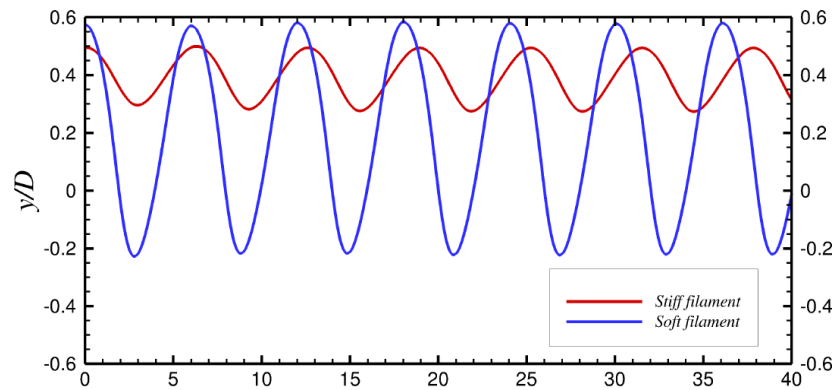
The boundary conditions at top and bottom of the computational domain are free-slip condition and the filament is maintained in position using the simply supported condition at the fixed end. The object is posed in a box with a uniform spacing of 60 per diameter and two different bending coefficients are tested. The parameters used in the simulation are summarised in table 3.5:

Hinged Filament behind a 2D Circular Cylinder		
Length in x -direction	L_x	21
Length in y -direction	L_y	10
Filament Length	L	1.5
Cylinder diameter	D	1.0
filament density	ρ_s	0.1
Bending Stiffness	K_b	$5 \times 10^{-3}, 0.1$
Reynolds number	$\frac{UD}{\nu}$	100
Richardson number	Ri	0.0
Initial angle	θ	0°
N° of Lagrangian points	N	84

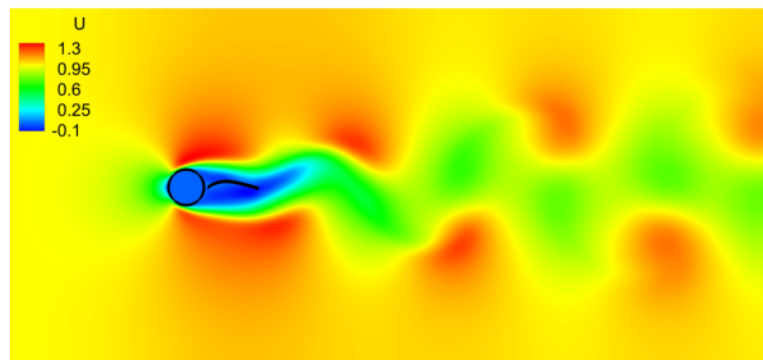
Table 3.5: Parameters used in the present simulations.

The simulations were run until a periodic flapping is observed and the time evolution of the free extremity of the filament is monitored. As figured out by Bagheri et al. ,

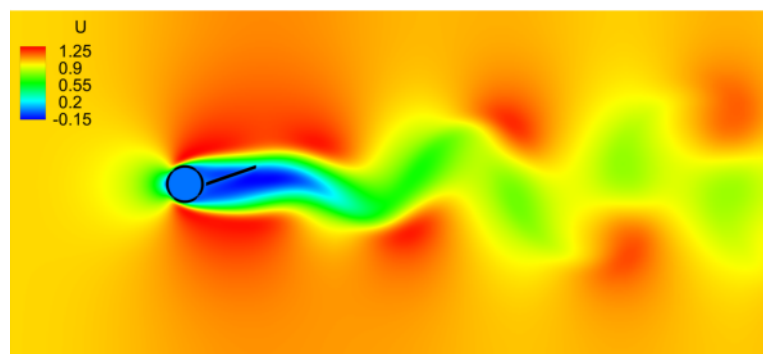
a clear symmetry breaking is observed. After a transient, in both cases, the filament starts to flap periodically in the upper part of the cylinder. The results are shown in figure 3.8:



(a)



(b)



(c)

Figure 3.8: Filament flapping behind a circular cylinder. (a) Free extremity time evolution. (b) Field snapshot of u velocity component for the softer filament (c) Field snapshot of u velocity component for the stiffer filament.

Little differences were found comparing the results with Bagheri et al. In particular a difference in flapping frequency of 4% and 7% for the softer and stiffer case, respectively, however, the physics of the problem is respected and symmetry breaking is clear for both cases and the above differences in frequency may be caused by the different immersed boundary method used for two cases compared.

Chapter 4

Results

In this chapter the results of the three dimensional simulations will be shown. A circular cylinder stands in an unperturbed uniform flow at $Re = 200$ and a series of flexible, inextensible filaments are clamped in the rear of the cylinder and are free to move in any space direction. The clamped condition is conveniently used instead of the simply supported condition because it is more realistic and closer to a possible future implementation of an anchoring system of the filaments in engineering applications such as in experiments.

The Reynolds number chosen is just above the three dimensionality threshold guaranteeing a three dimensional flow and, at the same time, allowing to visualize the effect of the filaments on the three dimensional bifurcation that may be affected by the presence of the flexible appendages.

The filaments are packed along the spanwise direction in two different ways:

- Sparse packing.
- Dense packing.

The sparse packing provides 8 equispaced filaments, whereas the dense packing provides 32 equispaced filaments. In the second case the space between the filaments is considerably reduced and this may have not negligible consequences on the dynamics of the wires.

For each of these arrangement of the filaments, the following parameters will be test:

- The length of the filaments L .
- The bending stiffness K_b .

In particular, as shown later, the bending stiffness is chosen according to the following criteria: in one case K_b is taken in order to accord the natural frequency of filaments, f_n , with frequency f_s of the vortex shedding, periodically generated by the detachment of the boundary layer from the upper and lower part of the cylinder. In the other case K_b is chosen in order to obtain a f_n double compared to f_s .

Two decreasing length of the filaments respect to the cylinder diameter will be tested. The length is reduced in the second case to try to recreate a possible symmetry-breaking scenarios that occurs in two dimension when the filament is short.

The density of each filament ρ_s is taken equal to 1 for convenience in all the simulations performed.

A summary of the simulations are performed is offered in table 4.1.

Summary of the simulations					
		N° of filaments	Re	ρ_s	L/D
Simulation	1	8	200	1.0	1.0
Simulation	2	32	200	1.0	1.0
Simulation	3	8	200	1.0	1.0
Simulation	4	32	200	1.0	1.0
Simulation	5	8	200	1.0	0.5
Simulation	6	8	200	1.0	0.5
Simulation	7	32	200	1.0	0.5

Table 4.1: List of the simulations performed.

4.1 Computational Domain

The choice of the computational domain is one of the most important things in CFD. On one hand, the domain must be sufficiently large to avoid the flow confinement and the manifestation of unwanted boundary effects that can significantly affect the solution and lead to incorrect results. On the other hand the computational grid must be fine enough to capture the flow structure and give a solution as accurate as possible, but always keeping in mind that a fine which is too fine grid has a huge impact on the computational time and cost.

The grid used for the present simulations is shown in figure 4.1. The domain size has been chosen referring to the literature, in particular with [14] and it is reported in table 4.2. The choice of a spanwise length of $\frac{L_z}{D} = 8$ is induced by the fact that the three dimensional instabilities described in chapter 1 have a wavelength of $\frac{\lambda_z}{D} \approx 4$ for the Mode A and $\frac{\lambda_z}{D} \approx 0.9$ for mode B. Thus, $\frac{L_z}{D} = 8$ is taken *a priori* in order to resolve well both these instabilities and simulate with only one grid all the cases to be study.

The grid is composed by an inner box with a uniform spacing in all the three cartesian directions containing the circular cylinder and the filaments. This choice has been done to guarantee the maximum accuracy in resolving the boundary layer detaching for the cylinder boundary and the motion of the filaments induced by vortex shedding. Out of the uniform spacing zone, the grid is stretched in the x and y directions following an exponential rule in order to save computational nodes where not necessary and to decrease the computational time. The grid spacing in the spanwise direction is taken constant and fine enough to resolve well the three dimensional flow behind the cylinder according to [14]. A the full grid setup can be found in table 4.2.

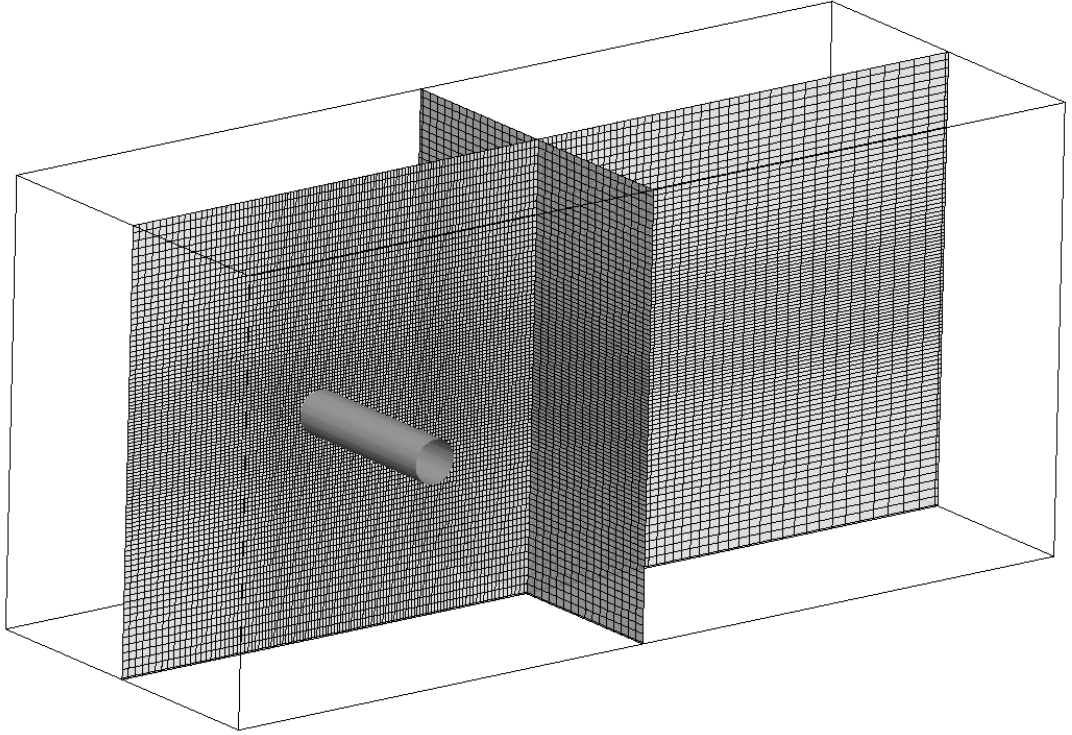


Figure 4.1: Grid used for the simulations. The grid is represented coarser to allow a better visualization.

Domain setup			
Domain size	$L_x \times L_y \times L_z$		$21.5 \times 10 \times 8$
N° of grid points	$N_x \times N_y \times N_z$		$482 \times 275 \times 98$
stretching factor in x -direction	r_x		1.005, 1.01
stretching factor in y -direction	r_y		1.01

<i>Uniform box zone</i>			
Domain size	$l_x \times l_y \times l_z$		$4v \times 2 \times 8$
N° of grid points per diameter	Ne		40

Table 4.2: Domain and grid setup for the simulations performed. The stretching factor $r_x = 1.01$ is used in the final part of the domain where less accuracy is needed.

The boundary conditions applied at the top and bottom of the domain are the free-slip conditions, while, at the boundary sides along the span, the periodic boundary conditions are used in order to take advantage of a FFT algorithm for a fast solution of the Poisson equation.

4.2 Choice of the Bending Stiffness

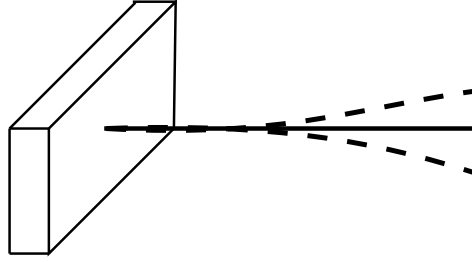


Figure 4.2: Free vibrations of undamped cantilever beam.

As introduced in the previous section, the bending stiffness is taken in order to accord the natural frequency of the filaments f_n with the vortex shedding frequency f_s or to render it double respect to f_s . The starting point to find the correct value of K_b is the free-filament equation, because only the natural frequency is needed:

$$\frac{\partial^2 Y}{\partial t^2} = -K_b \frac{\partial^4 Y}{\partial s^4} \quad . \quad (4.1)$$

Equation (4.1) is the well know dimensionless Euler-Bernoulli equation for an elastic beam. Only the y -component of the equation is considered because the resonating condition is sought only for the streamwise disturbance associated with the vortex shedding and not with the spanwise instability that is less powerful.

The normal mode solution to the equation (4.1) becomes:

$$Y(s, t) = F(s)G(t) \quad , \quad (4.2)$$

Substituting in (4.1) the equation become:

$$F(s) \frac{d^2 G(t)}{dt^2} = K_b \frac{d^4 F(s)}{ds^4} G(t) \quad . \quad (4.3)$$

From the above equation, after some manipulation, the equation for the displacement in wall-normal direction reads:

$$F(s) = C_1 \cos(\beta_n s) + C_2 \sin(\beta_n s) + C_3 \cosh(\beta_n s) + C_4 \sinh(\beta_n s) \quad , \quad (4.4)$$

where $\beta_n = \left(\frac{\omega^2}{K_b}\right)^{\frac{1}{4}}$.

The boundary conditions for a filament clamped at the one end, as shown in figure 4.2, are:

Boundary conditions	
$s = 0$	$s = L$
$Y = 0$	$\frac{d^2 Y}{ds^2} = 0$
$\frac{dY}{ds} = 0$	$\frac{d^3 Y}{ds^3} = 0$

Applying the boundary conditions, the following equation is to be solved:

$$\cos(\beta L)\cosh(\beta L) = -1 \quad . \quad (4.5)$$

The roots of the above equation are:

Roots of the equation 4.5	
n	$\beta_n L$
1	1.8751
2	4.69409
3	7.85475
4	10.99554
5	14.13176

The value of β_n are needed in the equation for the time, that reads:

$$G(t) = b_1 \sin(\beta_n^2 \sqrt{K_b} t) + b_2 \cos(\beta_n^2 \sqrt{K_b} t) \quad , \quad (4.6)$$

The coefficients b_1 and b_2 are to be determined using initial conditions and their expression in of no importance here.

The natural frequency is:

$$f_n = \frac{\beta_n^2}{2\pi L^2} \sqrt{K_b} \quad . \quad (4.7)$$

The first value of natural frequency is therefore: $f_1 = \frac{3.516}{L^2} \sqrt{K_b}$. The value of bending stiffness to use in the simulations can be obtain simply rearranging the previous expression for f_1 as:

$$K_b = \frac{(2k\pi f_s L^2)^2}{3.516^2}, \quad k = 1, 2 \quad , \quad (4.8)$$

where f_s is the shedding frequency measured from the fluctuation in time of the lift coefficient and k is a factor used to module the the shedding frequency f_s in order to obtain the wanted value of f_n .

4.3 Simulation Cases: $L/D = 1$

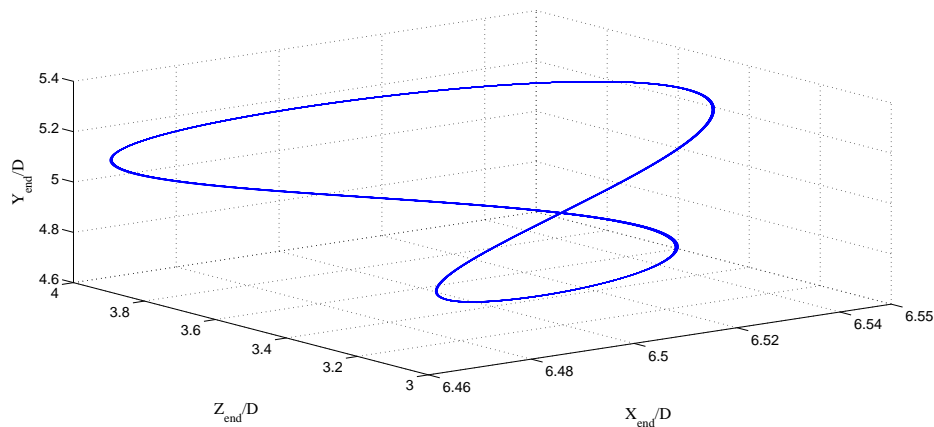
The simulation cases with $L/D = 1$ are the first tackled and, as described before, four different configurations will be tested. For each configuration the aerodynamic performance will be measured and the dynamics of the filament in the space will be shown. A summary of these simulations is offered in table 4.3:

Summary of the simulations						
		N° of filaments	Re	ρ_s	f_n/f_s	K_b
Simulation	1	8	200	1.0	1.0	0.13
Simulation	2	32	200	1.0	2.0	0.52
Simulation	3	8	200	1.0	1.0	0.13
Simulation	4	32	200	1.0	2.0	0.52

Table 4.3: summary of simulation performed for the case $L/D = 1$.

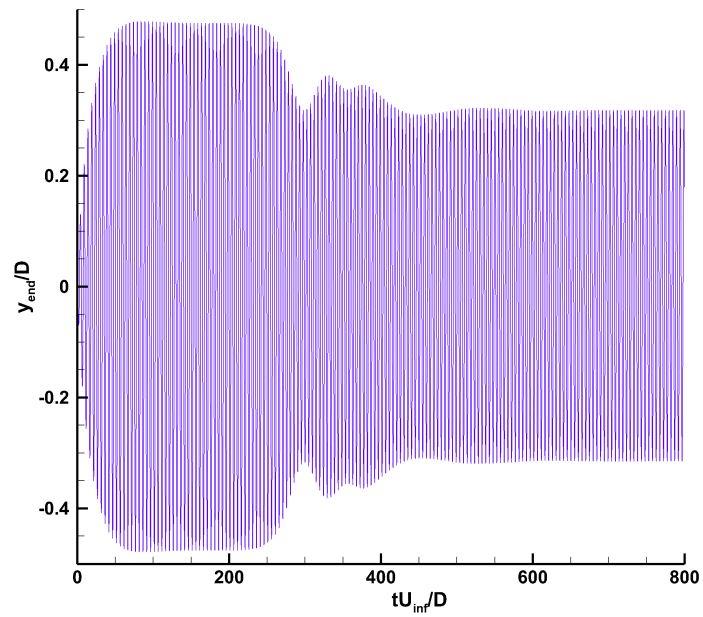
4.3.1 Dynamics of the Filaments behind the Cylinder

Starting from the sparse filaments packing, this case offer an interesting behaviour not simply predictable. The filaments are aligned along the spanwise direction with a distance between each appendage of $\frac{\Delta z}{D} = 1$ and with an initial angle of 0° relatively to the flow direction, from left to right. The filaments are free to flap under the action of the forces that the fluid exerted over the immersed bodies and, because of the three dimensional nature of the flow, a motion in spanwise direction is expected. As in two dimensional simulations, the free extremity of the appendages is taken as a reference of the motion of the filaments in space. The results for the resonating case, with $K_b = 0.13$, are plotted in figure 4.4.

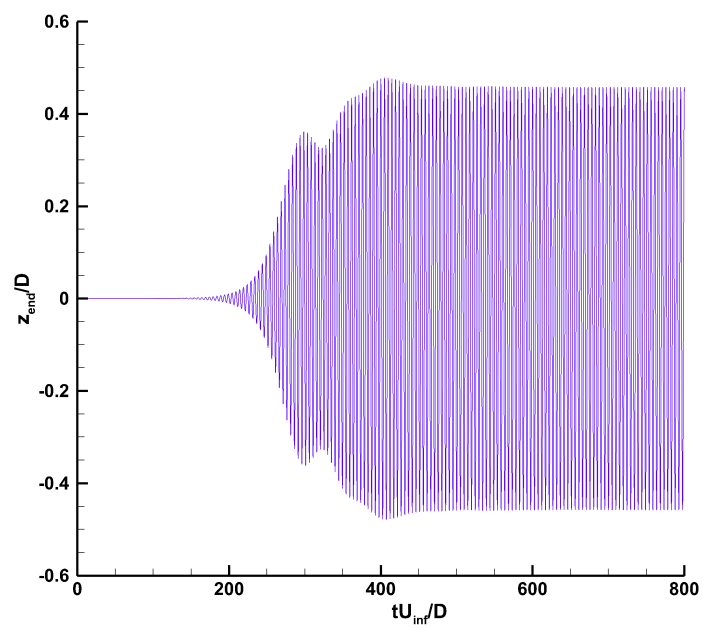
Figure 4.3: Positions by the middle filament during its motion. The number of filament is 8 and $K_b = 0.13$.

The filaments move synchronised in $x-y$ plane increasing the amplitude of oscillations, until reaching a self sustained flapping state. The spanwise motion is characterized by a transient that leads to large oscillations and, as shown in figure 4.5, each two filaments move in phase, giving rise to an interesting dynamics.

In figure 4.3 is shown the trajectory followed by free extremity of the middle filament (filament n°4); this trajectory draws in the space an eight-like orbit, similar to the two dimensional case.



(a)



(b)

Figure 4.4: Free extremity time evolution for $K_b = 0.13$ and 8 filaments. (a) y -component of displacement. (b) z -component of displacement.

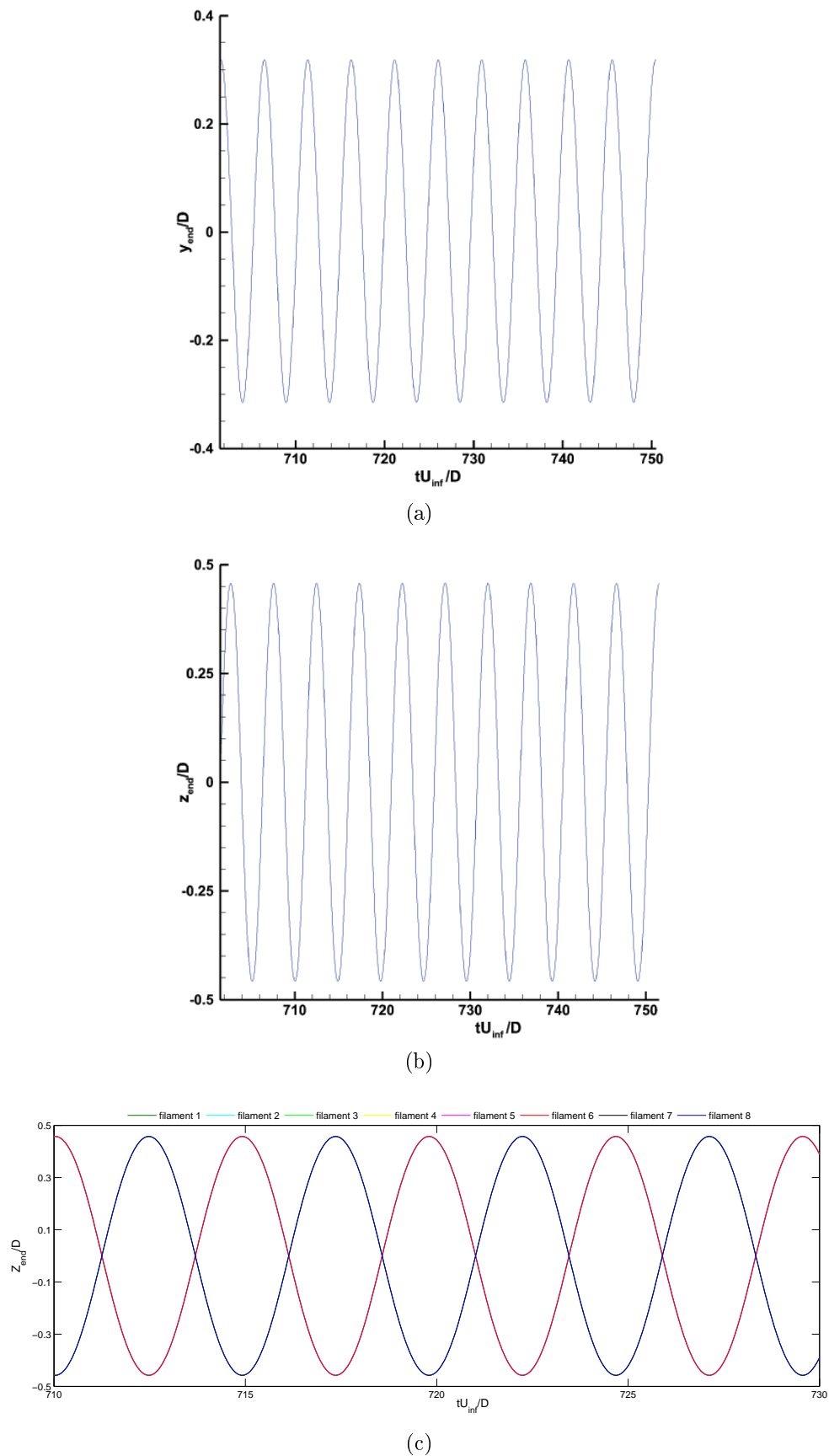


Figure 4.5: Detailed view of the self-sustained oscillations. (a) y -component of displacement, (b) z -component of displacement, (c) Superposition of the z -component of displacement for all the filaments.

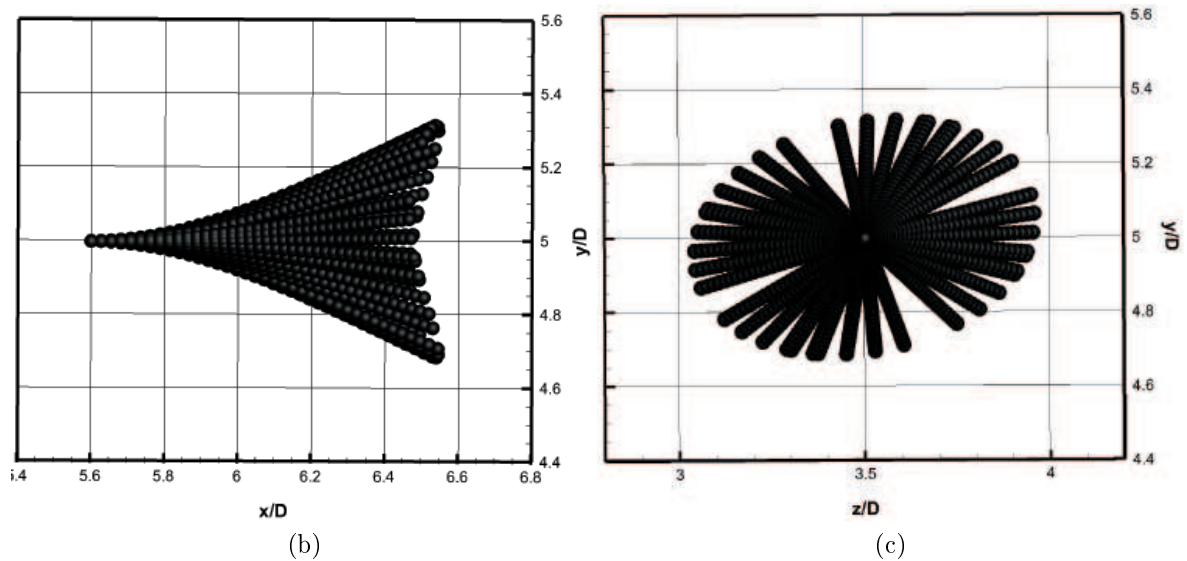
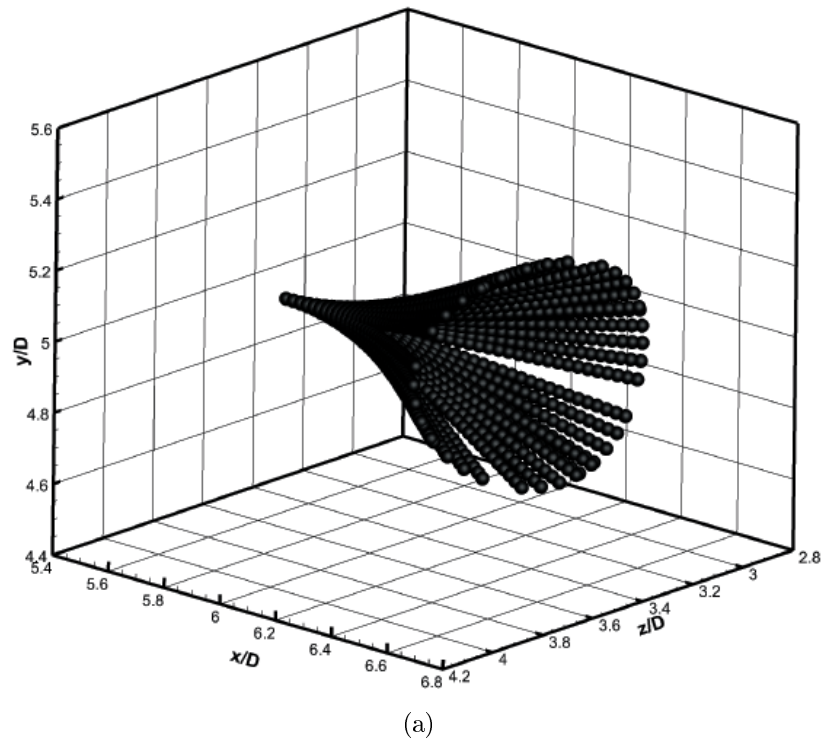
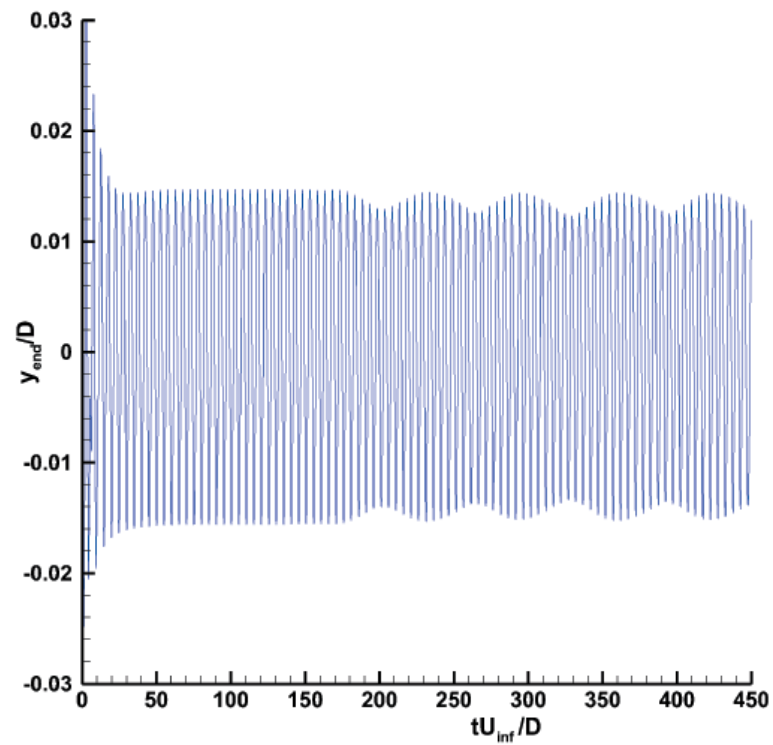
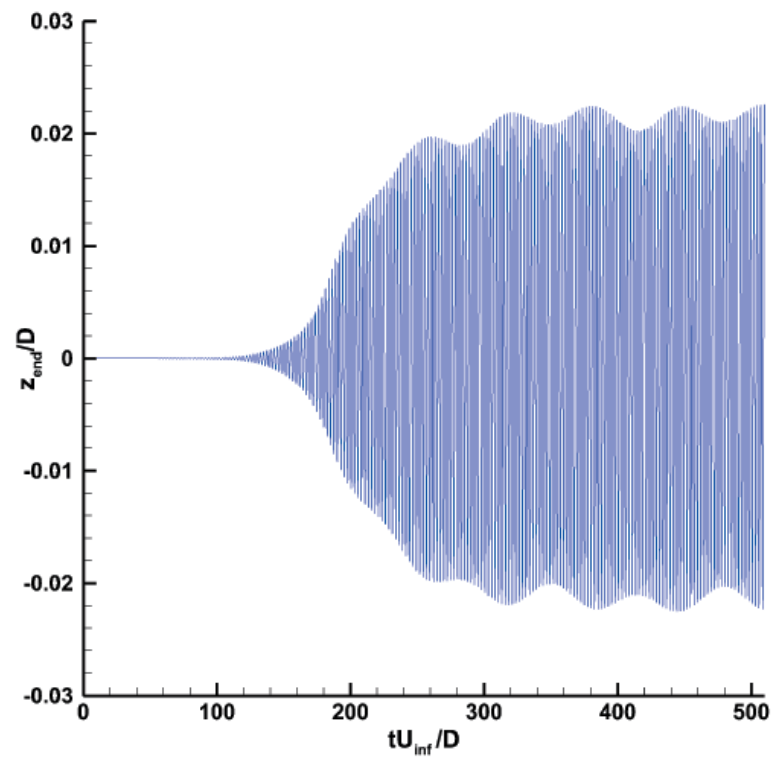


Figure 4.6: Sketch of the positions assumed by the middle the filament for $K_b = 0.13$; case with 8 filaments. (a) Isometric view. (b) $x-y$ plane view. (c) $z-y$ plane view.

The stiffer case, with $K_b = 0.52$, as predictable, is characterized by smaller oscillation in each direction because of the larger value of the bending stiffness, that also avoid the matching between the natural frequency of the filament and the flow. However the dynamic of the motion is similar, presenting a transient with increasing oscillations in each space direction. The path of the free end and is proposed in figure 4.9.



(a)



(b)

Figure 4.7: Free extremity time evolution for $K_b = 0.52$; 8 filaments. (a) y -component of displacement, (b) z -component of displacement.

The sparse packing allows the motion of the filaments in spanwise direction, but this degree of freedom is lost if the number of filaments is increased to 32. The spacing between the appendages is now $\Delta z = 0.25$ and this restriction inhibits the motion of the filaments, forcing them to flap only in x - y plane, as show in figure 4.8. Moreover, as shown in figure 4.9, in comparison with the sparse arrangement, closely spaced filaments flap at smaller amplitude.

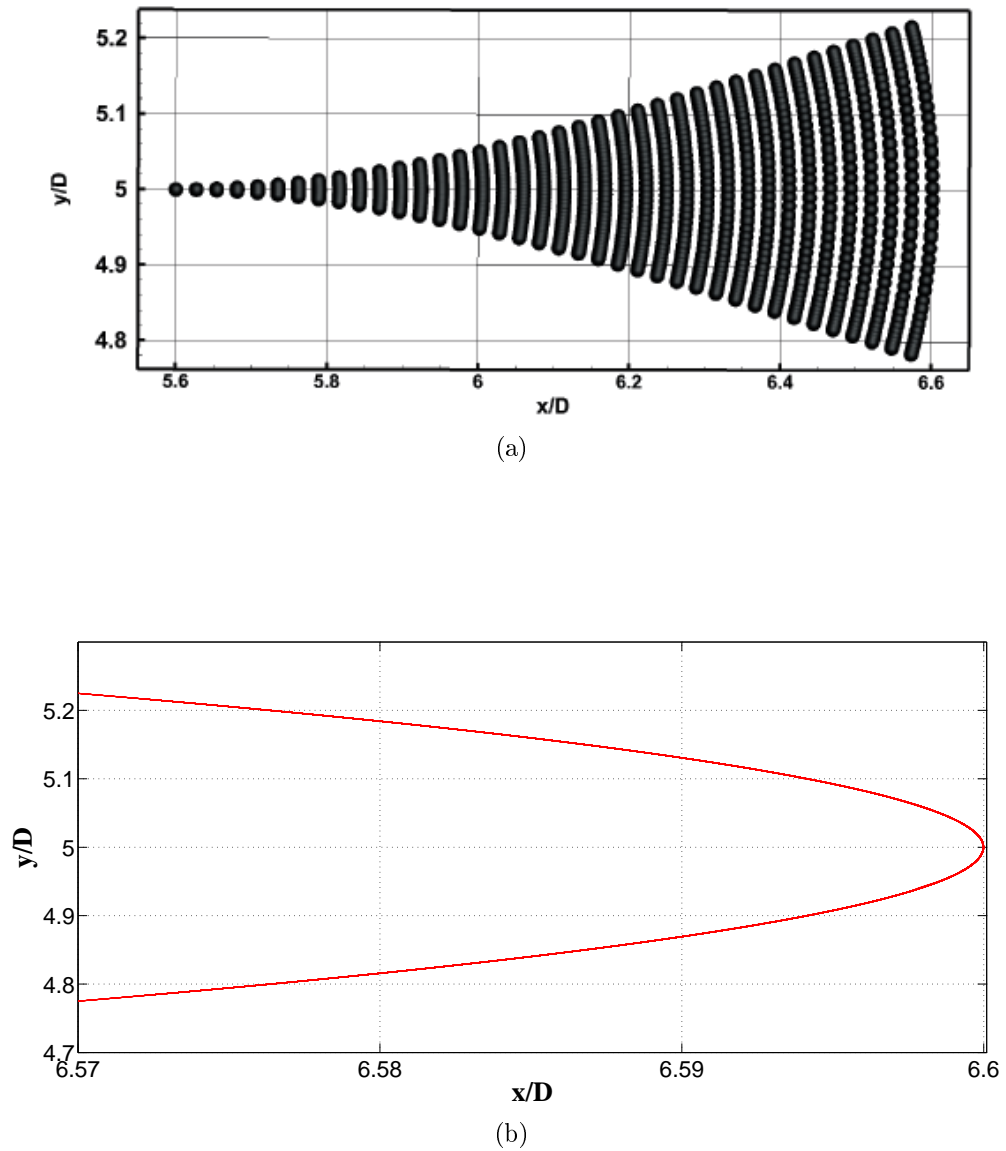
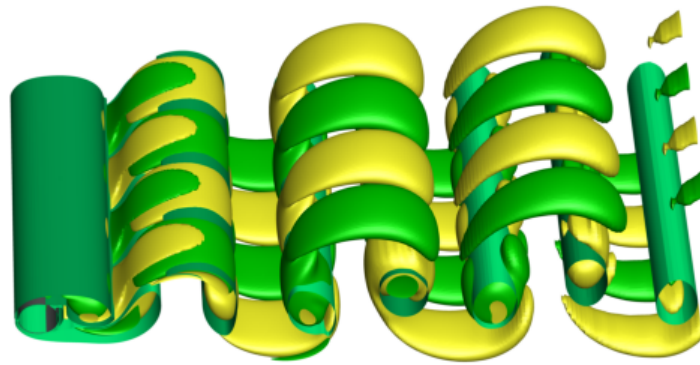


Figure 4.8: Sketch of the positions assumed the middle filament for $K_b = 0.13$; case with 32 filaments. (a) x - y plane view, (b) positions reached by the end point of the central filament.

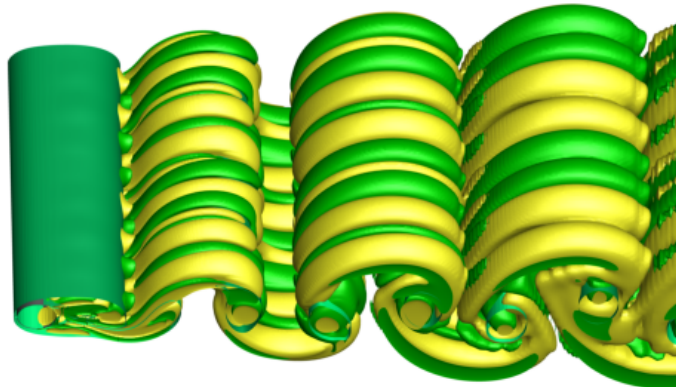
4.3.2 Effect On The Cylinder Wake



(a)



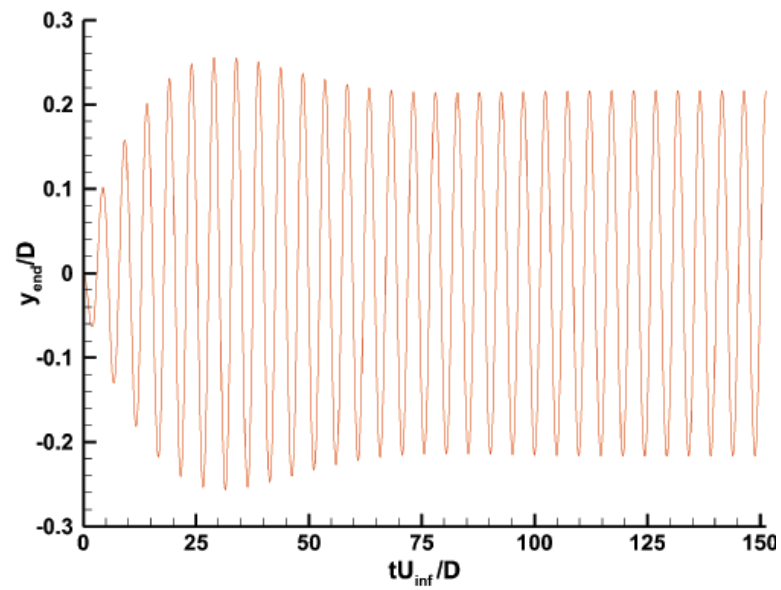
(b)



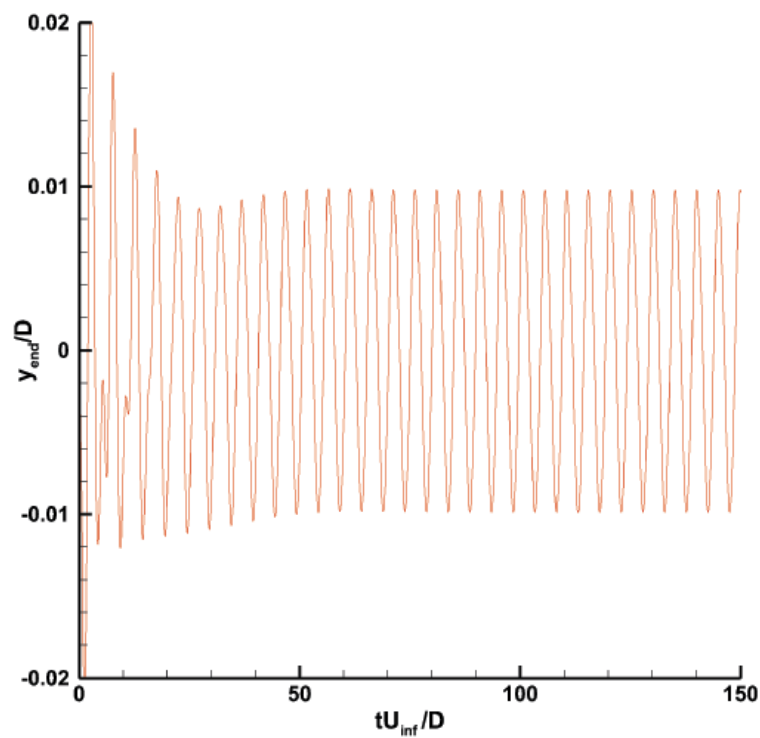
(c)

Figure 4.10: Wake structure behind the cylinder at $Re = 200$. Iso-surface of positive (green) and negative (yellow) ω_x vorticity; in red and violet the iso-surface of negative and positive ω_z vorticity are shown, (a) Cylinder wake without filaments, (b) first bifurcation of the cylinder wake with 8 filaments and $K_b = 0.13$, (c) Final structure of the cylinder wake with 8 filaments and $K_b = 0.13$.

The presence of the flexible filaments behind the cylinder has important effects on the wake structure. In chapter 1, the main bifurcation and the structure of the cylinder wake was introduced and it was underlined how the wavelength of the three dimensional



(a)



(b)

Figure 4.9: Free extremity time evolution for the 32 filaments case, (a) y -component of displacement, $K_b = 0.13$, (b) y -component of displacement, $K_b = 0.52$.

instabilities changed in relation to the Reynolds number. The simulations in the present work are performed beyond the three dimensionality threshold but, however, before the second bifurcation for the base cylinder case, which occurs at $Re = 260$.

The presence of the filaments acts on the flow and contributes to introducing instabilities that change the shape of wake. In figure 4.10 the wake structure for the cylinder with 8 filaments and $K_b = 0.13$ is shown. The presence of the appendages cause two consecutive transition in the wake: the first one occurs when the spanwise motion is not fully stabilized. The filaments anticipate the second bifurcation leading to a mode B shape with the formation of streamwise vortex pairs with a spanwise wavelength $\lambda_z = 8$ (see figure 4.10(b)).

The second one takes place when the filaments reach their limit cycle. The motion in each direction of the filaments, moving two by two in phase, introduces new wave length in the instabilities leading to a new wake structure characterized by a spanwise wavelength λ_z of almost 6 (see figure 4.10(c)).

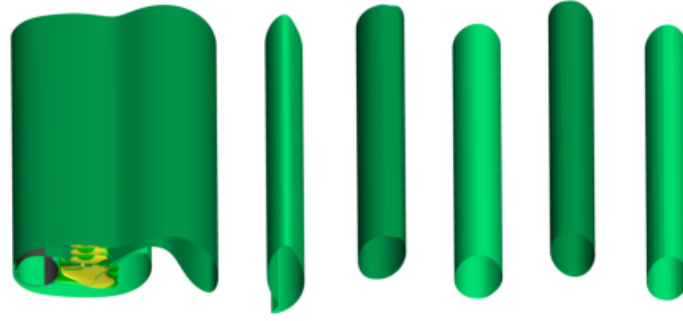
For $K_b = 0.52$ a similar scenario occurs: the second three dimensional bifurcation is anticipated and a mode B shedding takes place instead of a mode A. However the small order of the oscillation does not cause a second transition and the spanwise wave length of the streamwise vortex pairs remains $\lambda_z = 8$, as shown if figure 4.11.



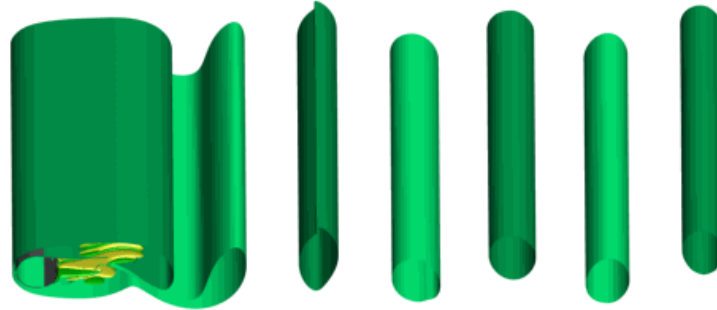
(a)

Figure 4.11: Wake structure behind the cylinder at $Re = 200$ with 8 filaments and $K_b = 0.52$. Iso-surface of positive (green) and negative (yellow) ω_x vorticity. in dark green and light blue the iso-surface of negative and positive ω_z vorticity are represented

Increasing the number of the filaments to 32, the effect on the wake structure become significant: the shedding modes A and B are inhibited. The streamwise vortex pairs that characterised the shedding mode A and B vanish and the ω_x vorticity component is localized only in the neighbourhood of the cylinder trailing edge, in correspondence to the dense packing of the filaments. The value of the bending stiffness does not play any role and the wake is affected by the filaments in a similar manner. The wake structure for both the cases with 32 filaments is shown in figure 4.12:



(a)



(b)

Figure 4.12: Wake structure behind the cylinder at $Re = 200$ with 32 filament. (a) $K_b = 0.13$, (b) $K_b = 0.52$. Iso-surface of positive (green) and negative (yellow) ω_x vorticity; in dark green and light blue the iso-surface of negative and positive ω_z vorticity are represented.

4.3.3 Effect on the Aerodynamic Coefficients

The aerodynamics coefficients are the main index of the aerodynamic performance of a body immersed in a flow. They are defined as the force in a specific direction, normalized with the dynamic pressure, as follow:

$$C_D = \frac{2F_x}{\rho_\infty U_\infty^2 S} \quad , \quad C_L = \frac{2F_y}{\rho_\infty U_\infty^2 S} \quad , \quad (4.9)$$

where S is the reference area of the object, taken as $S = L_z \times D$.

C_D is called drag coefficient and measure the drag suffer by the immersed body, whereas the lift coefficient C_L measure how much the fluid pushes the body in the direction normal to drag direction. The computed coefficients will be compared with the cylinder without filaments.

The forces exerted by the fluid over the entire body (cylinder+filaments) are computed performing a global momentum balance over the computational domain.

The effect of the filaments is surprising positive and the results are shown in figure 4.13. A comparison between all the cases with $L/D = 1$ is offered in figure 4.14.

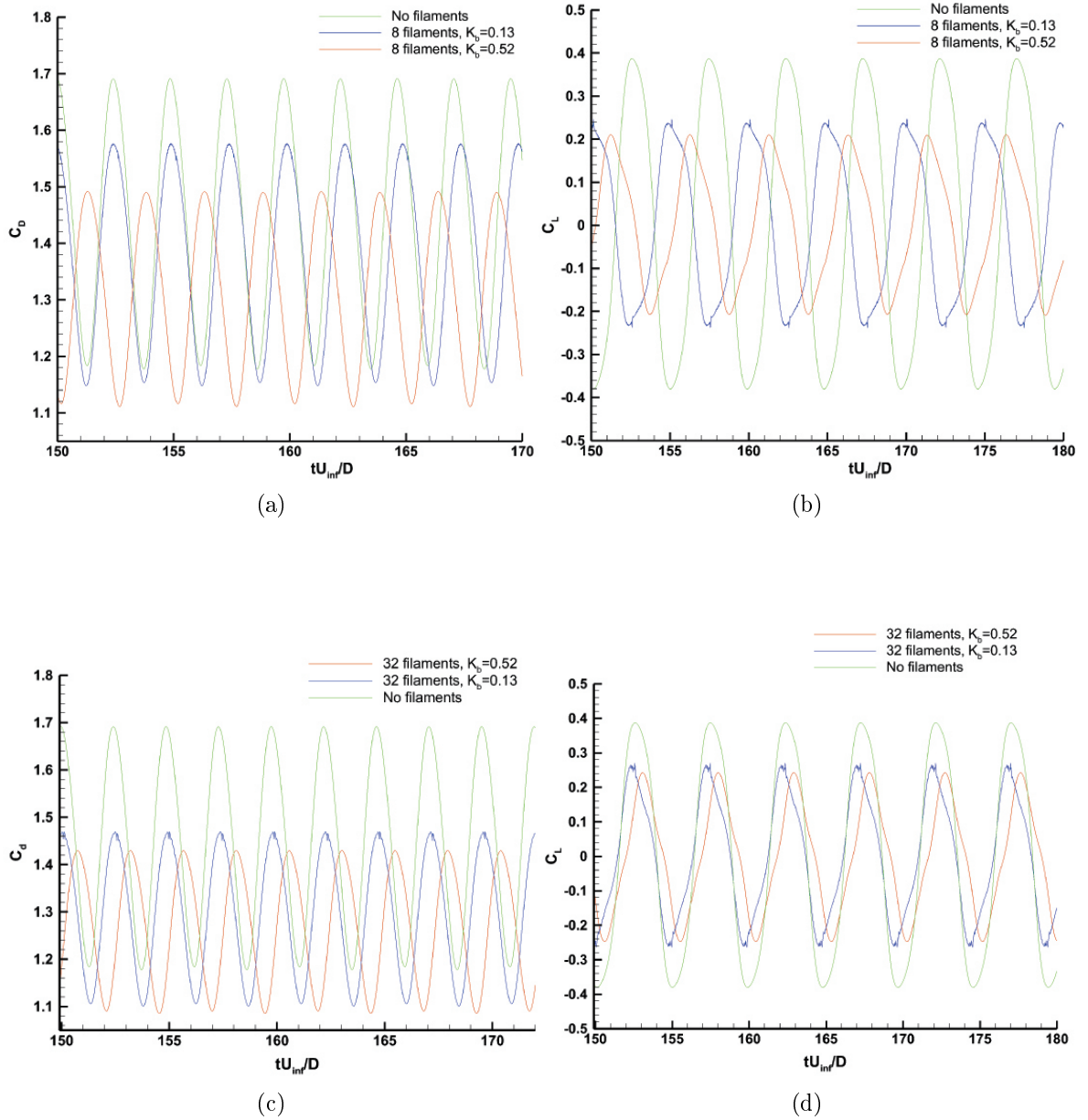
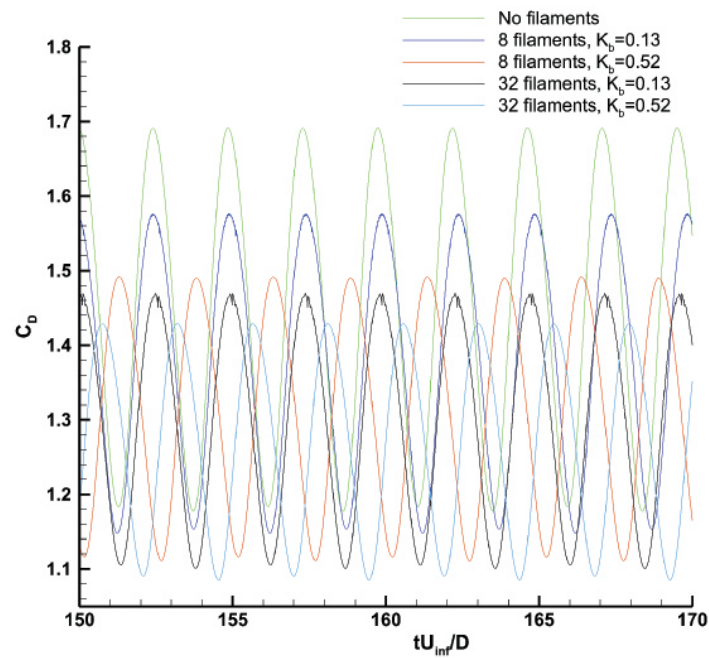
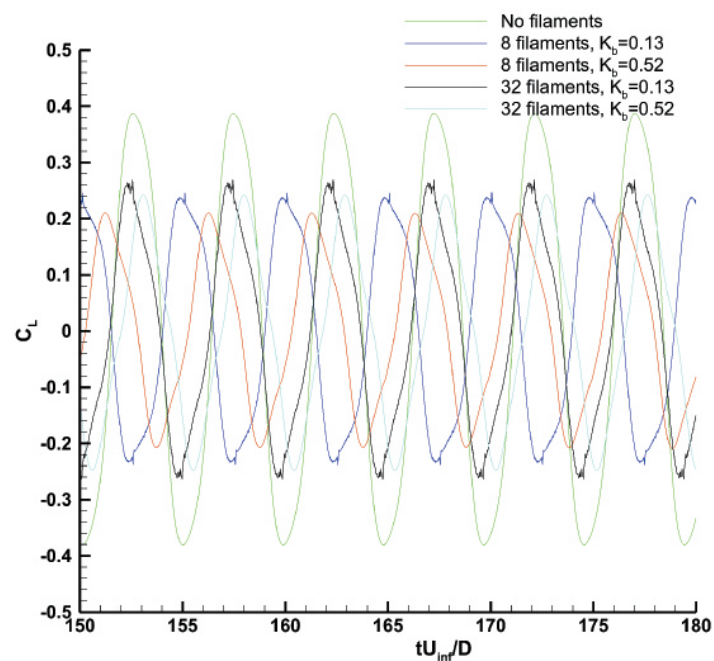


Figure 4.13: Aerodynamic effect of the filaments. (a) C_D comparison between the cases with 8 filaments and the cylinder without filaments; (b) C_L comparison between the cases with 8 filaments and the cylinder without filaments; (c) C_D comparison between the cases with 32 filaments and the cylinder without filaments; (d) C_L comparison between the cases with 8 filaments and the cylinder without filaments.



(a)



(b)

Figure 4.14: Comparison between all the cases with $L/D = 1$; (a) drag coefficients C_D ; (b) lift coefficients C_L .

The mean value of the coefficients and the root mean square values of the oscillation around the mean are collected and summarized in table 4.4:

Aerodynamic coefficients					
Case	K_b	$\overline{C_D}$	C'_{Drms}	$\overline{C_D}$	C'_{Lrms}
No filaments	–	1.448	0.0	0.180	0.290
8 filaments	0.13	1.343	0.0	0.133	0.228
8 filaments	0.52	1.315	0.0	0.147	0.216
32 filaments	0.13	1.296	0.0	0.128	0.173
32 filaments	0.52	1.268	0.0	0.120	0.157

Table 4.4: Summary of the aerodynamics coefficients for the cases with $L/D = 1$.

The benefits of the filaments is clear: the drag is decrease up to 12.5% and the *rms* lift coefficient oscillations are reduced up to 30%.

4.4 Simulation cases: $L/D = 0.5$

The simulation cases with $L/D = 0.5$ are summarized in table 4.5:

Summary of the simulations						
		N° of filaments	Re	ρ_s	f_n/f_s	K_b
Simulation	1	8	200	1.0	1.0	0.008
Simulation	2	32	200	1.0	1.0	0.008

Table 4.5: Summary of the simulations performed for the case $L/D = 0.5$.

4.4.1 Dynamics of the Filaments behind the Cylinder

The shorter filaments are tested in order to look at a possible symmetry-breaking scenario that, in two dimensions, occurs only if the appendage is sufficiently short with respect to the recirculation bubble generated behind the cylinder. However, in three dimensions this phenomenon is not granted and these simulations have the aim of testing the above described possibility. Also in this case the number of filaments tested is either 8 or 32.

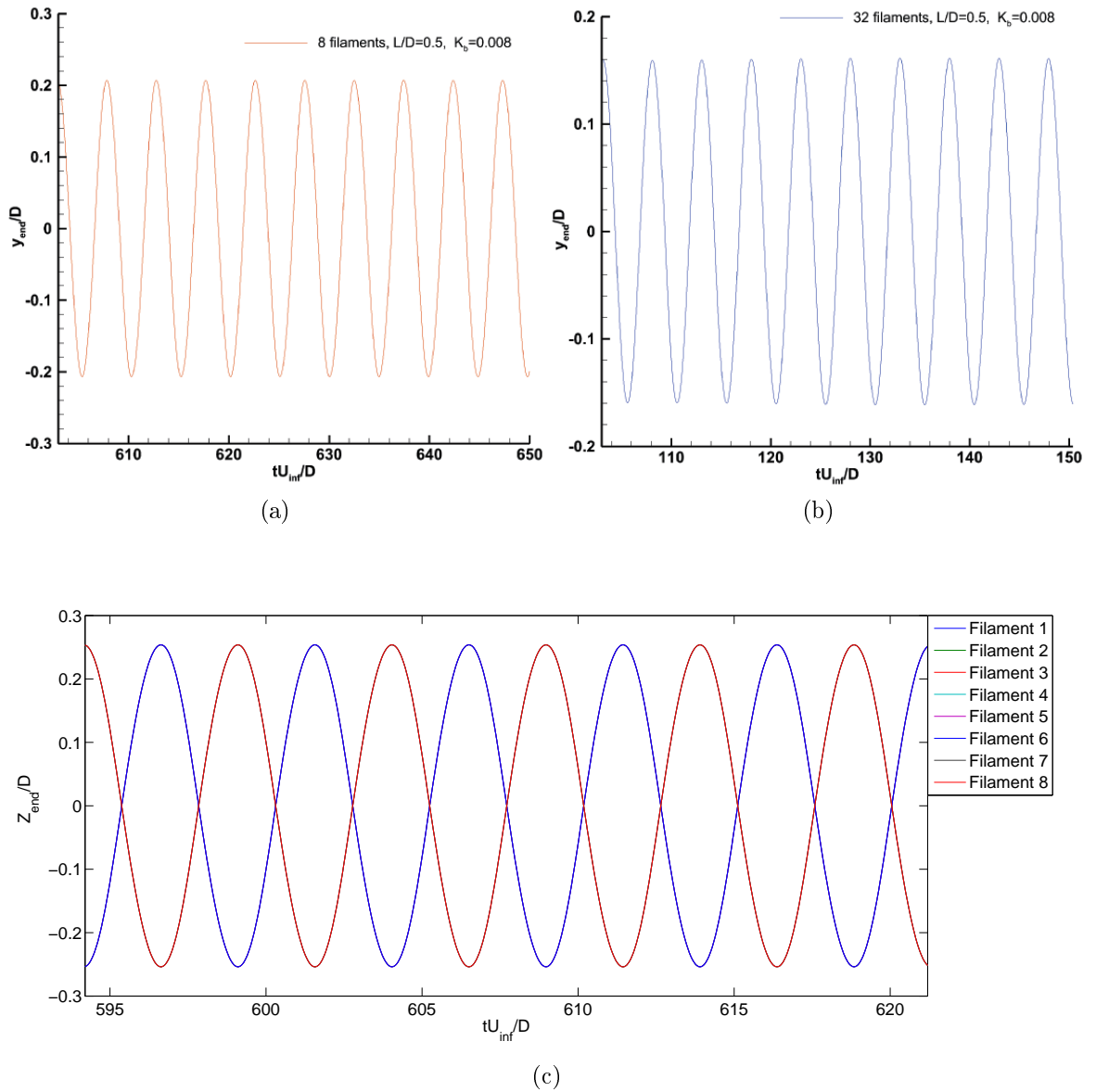


Figure 4.15: Time evolution of the free extremity, $L/D = 0.5$; (a) 8 filaments, y -component; (b) 32 filaments, y -component; (c) 8 filaments, superposition of z -component of the eight filaments.

The time evolution of the free extremity, shown in figure 4.15, helps to describe the dynamics of the shorter filaments. The appendages move in phase in x - y , in analogy with the cases with $L/D = 1$. The motion in the spanwise direction, that develops for the sparse arrangement, is in phase each two filaments and it is reported in figure 4.15 (c).

Increasing the number of filaments to 32, similar observation to cases with the longer filaments can be done. There is an inhibition of the spanwise motion of the filaments and the motion in x - y becomes regular and periodic in time after a short transient, as shown in figure 4.15 (b).

4.4.2 Effect on the Aerodynamic Coefficients

Previously it was found that the filaments have a positive impact on the aerodynamics of the entire body; also with the shorter filaments a decrease in drag and in lift force oscillations can be observed. The results are offered and compared together in figure 4.18 while the mean value of the coefficients and the root mean square of the oscillation with respect to the mean is proposed below in table 4.6:

Aerodynamic coefficients					
Case	K_b	$\overline{C_D}$	C'_{Drms}	$\overline{C_L}$	C'_{Lrms}
No filaments	–	1.448	0.0	0.180	0.290
8 filaments	0.008	1.385	0.0	0.158	0.208
32 filaments	0.008	1.350	0.0	0.142	0.142

Table 4.6: Summary of the aerodynamics coefficients for the cases with $L/D = 0.5$.

Because there is not a symmetry breaking, the C_L coefficient is symmetric with respect to the zero value, but, however, there is a good amelioration of the aerodynamic performance even if, fixing the number of filaments, slightly better results are obtain with $L/D = 1$.

4.4.3 Other simulations

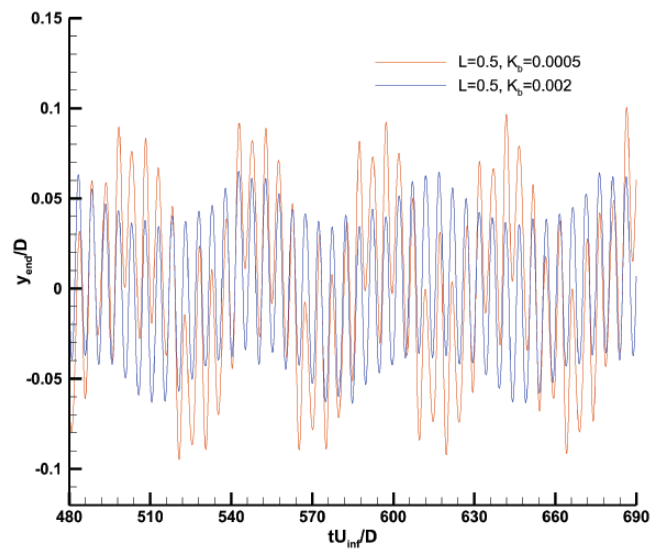
Other simulations with values of K_b not resonating with the flow and $L/D = 0.5$ were tested; the cases are summarized in table 4.7:

Summary of the simulations					
	N° of filaments	Re	ρ_s	K_b	
Simulation 1	8	200	1.0	0.0005	
Simulation 2	8	200	1.0	0.002	
Simulation 3	32	200	1.0	0.002	

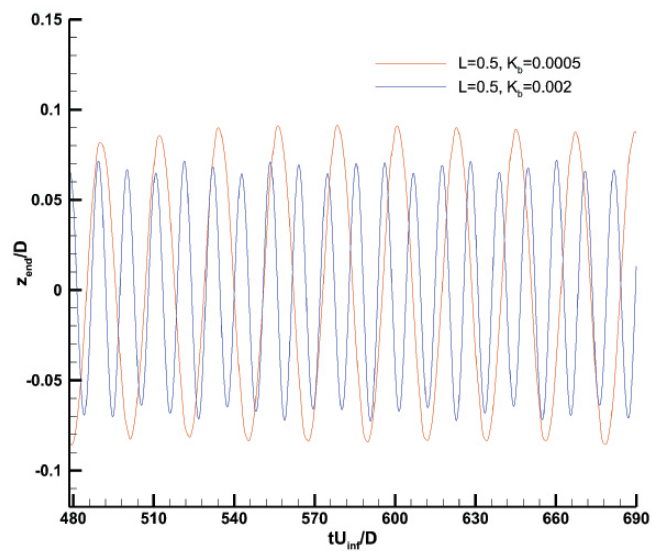
Table 4.7: Summary of the simulations performed for the case $L/D = 0.5$.

The softer values chosen for the bending stiffness give rise to a some differences respect with the previous cases. The filaments move again in phase in $x-y$ but their motion is composed by more frequencies and the filaments move alternatively in the lower and in the upper side of the cylinder. The motion in the spanwise direction, that develops for the sparse arrangement, is not in phase for all the filaments and it is reported in figure 4.17.

Increasing the number of filaments to 32, there is a regularization of the oscillations that becomes periodic in time after a small transient, as shown in figure 4.16 (c).



(a)



(b)

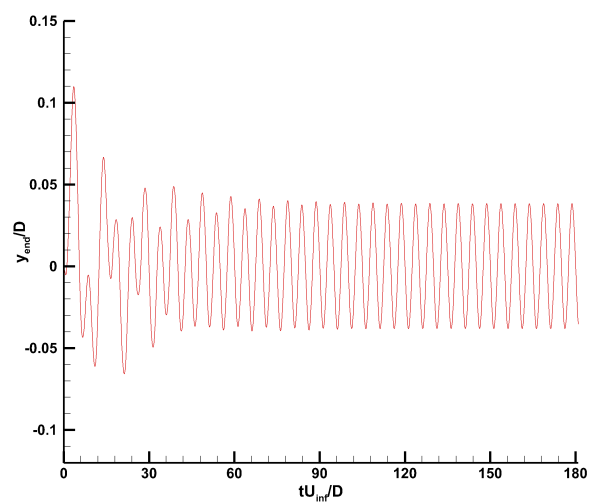
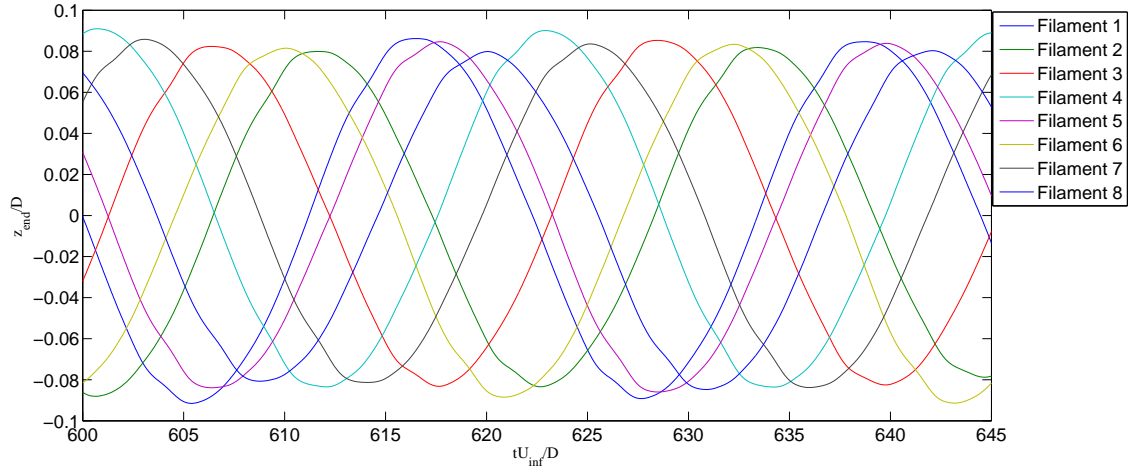
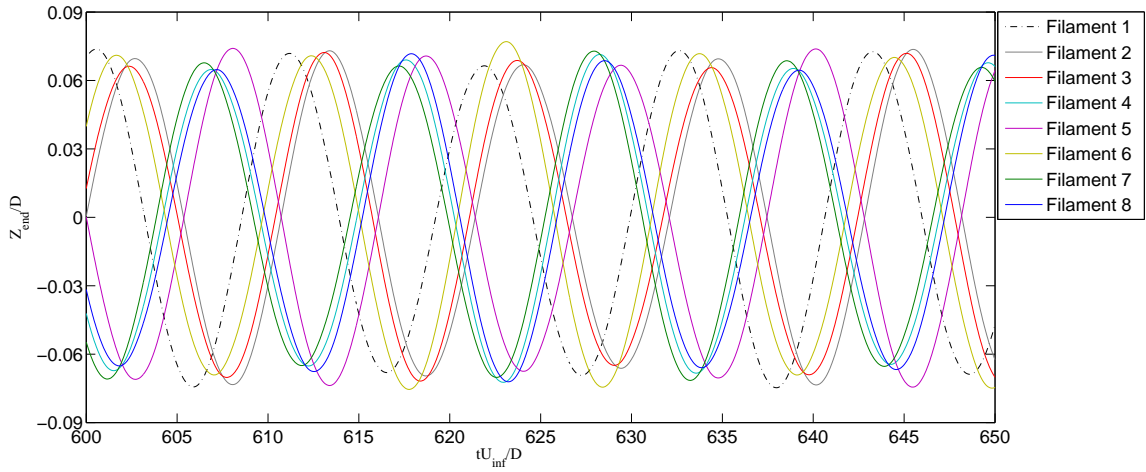


Figure 4.16: Time evolution of the free extremity, $L/D = 0.5$; (a) 8 filaments, y -component; (b) 8 filaments, z -component; (c) 32 filaments, y -component.



(a)



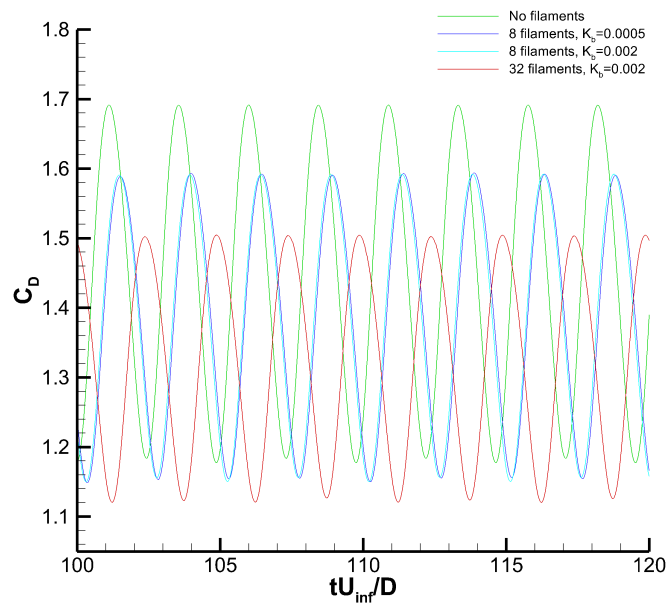
(b)

Figure 4.17: Time evolution of the z -component of the free extremity of the eight filaments; (a) $K_b = 0.0005$, (b) $K_b = 0.002$.

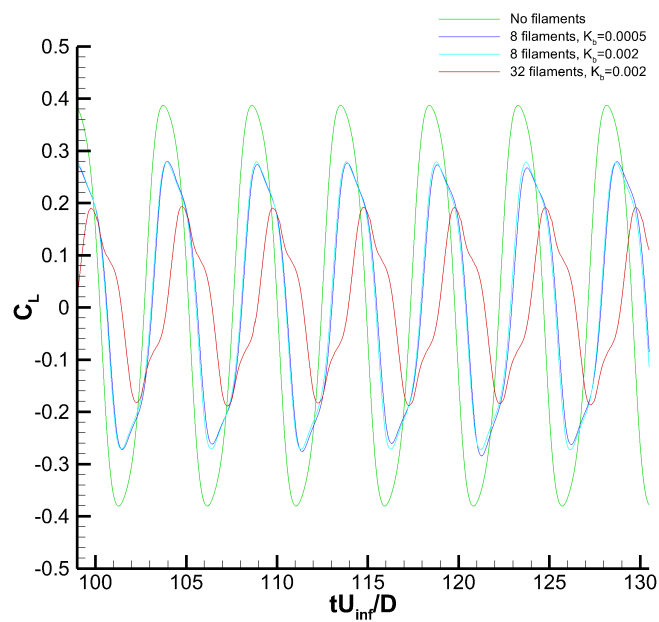
The computed aerodynamic coefficients are offered and compared together in figure 4.18 while the mean value of the coefficients and the root mean square of the oscillation with respect to the mean is proposed below in table 4.8:

Aerodynamic coefficients					
Case	K_b	$\overline{C_D}$	$\overline{C_L}$	C'_{Drms}	C'_{Lrms}
No filaments	—	1.448	0.0	0.180	0.290
8filaments	0.005	1.387	0.0	0.155	0.200
8filaments	0.002	1.388	0.0	0.155	0.201
32filaments	0.002	1.326	0.0	0.122	0.173

Table 4.8: Summary of the aerodynamics coefficients for the non resonant cases.



(a)



(b)

Figure 4.18: Comparison between all the cases with $L/D = 0.5$.(a) Drag coefficients C_D .(b) Lift coefficients C_L .

Chapter 5

Conclusions

The flow past a three-dimensional circular cylinder, equipped with a series of flexible, inextensible filaments clamped at the cylinder trailing edge and regularly spaced along the span has been simulated.

The filaments have been tested in two main configurations:

- Sparse packing: 8 filaments, over the length of the cylinder.
- Dense packing: 32 filaments, over the length of the cylinder.

The bending stiffness of the filaments has been chosen in order to make the natural frequency of the appendages close to the frequency of the vortex shedding, generated by the detachment of the boundary layer from the wall of the cylinder. For each of the above arrangements two different lengths of the filaments have been tested and the dynamics of the filaments has been monitored in time.

After analysing the results, the following conclusions can be made:

- The sparse packing allows the motion of the filaments in the spanwise direction for both "short" and "long" filaments.
- The dense packing totally inhibits the generation of the spanwise motion of the filaments. The appendages move in phase only in $x-y$ plane and flap at lower amplitude than in the sparse packing case. A full comparison of the motion of the filaments is offered in figure 5.1.
- The filaments act on the flow interacting with the wake and leading to changes in the wake shape as compared to the bare cylinder case. On one hand, the sparse packing of filaments anticipates the transition to the second three-dimensional bifurcation (Mode B instability), or it introduces disturbances that cause a reorganization of the mode A instability into a configuration with a lower wavelength. In particular, this second scenario can be found if the spanwise motion of the filament becomes relevant. On the other hand, the dense packing of filaments causes a radical change in the wake, suppressing totally the first bifurcation mode. The length of the filaments does not play a significant role in this transition process.

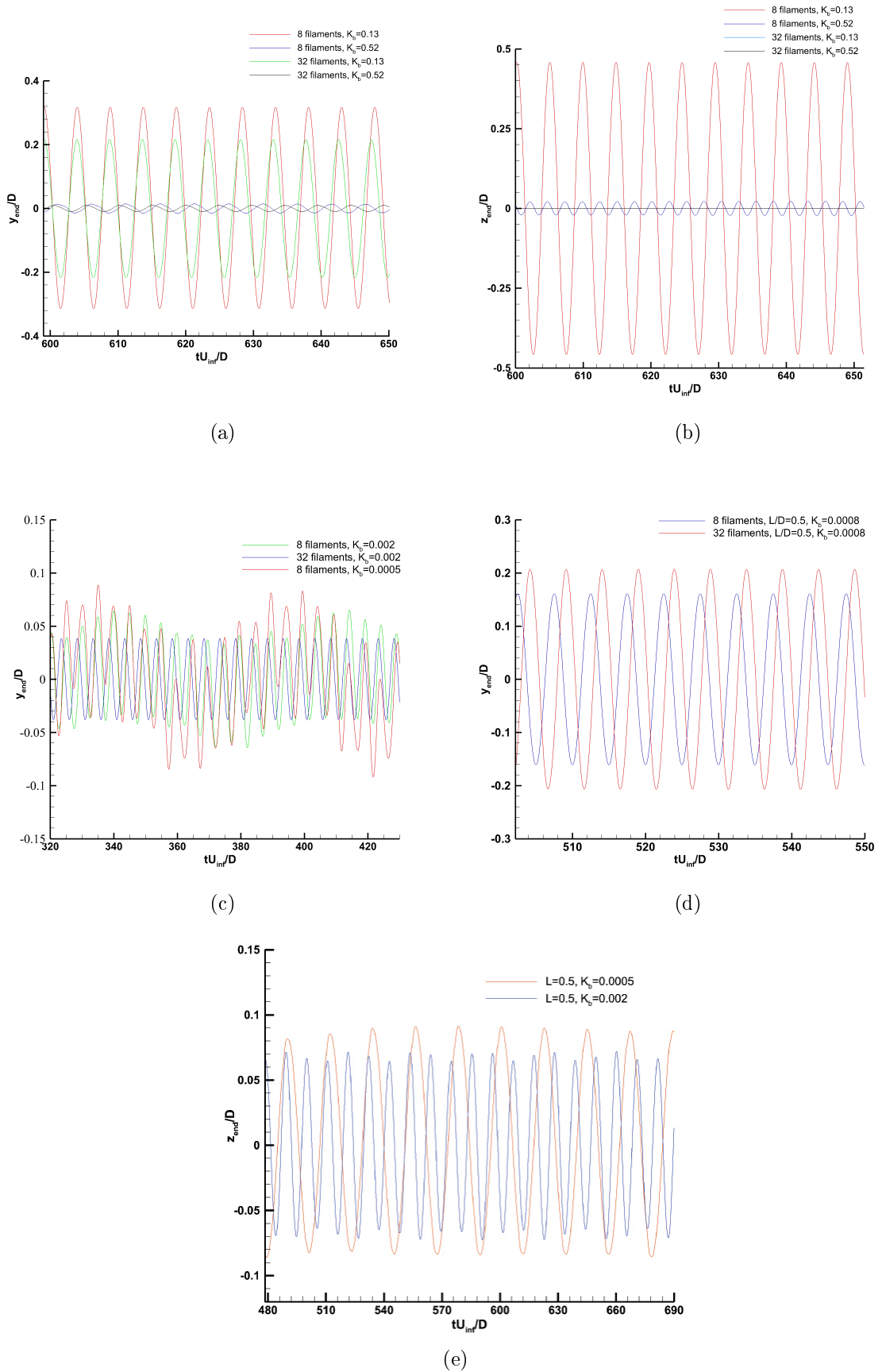


Figure 5.1: Comparison between displacement of the middle filaments. (a) y -component of the displacement. Case with $L/D = 1$; (b) z -component of the displacement. Case with $L/D = 1$; (c)-(d) y -component of the displacement. Case with $L/D = 0.5$; (d) z -component of the displacement. Case with $L/D = 0.5$.

- The aerodynamic performances are improved by the presence of the filaments. A decrease in drag up to 12.5% and a decrease in amplitude of lift oscillations up to 30% has been observed.

Summary of the computed aerodynamics coefficients

Case	L/D	K_b	$\overline{C_D}$	$\overline{C_L}$	$C'_{D_{rms}}$	$C'_{L_{rms}}$
No filaments	0.5	–	1.448	0.0	0.180	0.290
8 filaments	0.5	0.008	1.385	0.0	0.158	0.208
8 filaments	0.5	0.0005	1.387	0.0	0.155	0.200
8 filaments	0.5	0.002	1.388	0.0	0.155	0.201
32 filaments	0.5	0.008	1.350	0.0	0.142	0.142
32 filaments	0.5	0.002	1.326	0.0	0.122	0.173
8 filaments	1.0	0.13	1.343	0.0	0.133	0.228
8 filaments	1.0	0.52	1.315	0.0	0.147	0.216
32 filaments	1.0	0.13	1.296	0.0	0.128	0.173
32 filaments	1.0	0.52	1.268	0.0	0.120	0.157

Table 5.1: Summary of the computed aerodynamics coefficients.

Slightly better results are obtained with the longer filaments. The symmetry breaking bifurcation has not been found yet, but more simulations have to be performed in order to figure out this possible scenario. In fact, it is very likely that a symmetry breaking bifurcation - if it exists - would be postponed in the 3D case (as compared to the 2D case) since the filaments have a third direction (z) where to escape.

Bibliography

- [1] J. Zhang, S. Childress, A. Libchaber & M. Shelley, *Flexible filaments in a flowing soap film as a model for one-dimensional flags in a two-dimensional wind*. Nature, 2000.
- [2] L. Zhu , C.S. Peskin , *Simulation of a flapping flexible filament in a flowing soap film by the immersed boundary method*. Journal of Computational Physics, 2002-Elsevier .
- [3] S. Bagheri, A. Mazzino & A. Bottaro, *Spontaneous Symmetry Breaking of a Hinged Flapping Filament Generates Lift* physical Review Letters, 2012.
- [4] , C. H. K. Willimason, *Vortex dynamics in the cylinder wake*. Annual review of fluid mechanics, 1996.
- [5] C.M. Rhie, W.L. Chow, *Numerical study of the turbulent flow past an airfoil with trailing edge separation*. AIAA Journal, 1983.
- [6] A.j. Chorin, *Numerical Solution of the Navier-Stokes Equations* Math. Comp. 22, pp. 745-762, 1968
- [7] J. Kim, P. Moin, *Application of a fractional-step method to incompressible Navier-Stokes equations.*, Journal of computational physics, 1985-Elsevier.
- [8] C.S. Peskin, *Numerical analysis of blood flow in the heart*. Journal of computational physics, 1977-Elsevier.
- [9] A. Pinelli, I.Z. Naqavi, U. Piomelli, J. Favier , *Immersed-boundary methods for general finite-difference and finite-volume Navier-stokes solvers.*, Journal of computational physics, 2010
- [10] A.M. Roma, C.S. Peskin, M.J. Berger, *An adaptive version of the immersed boundary method.*, Journal of Computational Physics, 153, pp. 509-534, 1999.
- [11] W.K. Liu, S. Jun, Y.F. Zhang , *Reproducing kernel particle methods*. International Journal for Numerical Methods in Fluids, vol.20 , pp. 1081-1106, 1995
- [12] Wei-Xi Huang, Soo Jai Shin, Hyung Jin Sung, *Simulation of flexible filaments in a uniform flow by the immersed boundary method.*, Journal of Computational physics, 2007.

-
- [13] J. Favier, A. Revell, A. Pinelli, *A Lattice Boltzmann-Immersed Boundary method to simulate the fluid interaction with moving and slender flexible objects.*, Journal of Computational Physics, 2014-Elsevier
- [14] V.A. GushchinCorresponding, A.V. Kostomarov, P.V. Matyushin, E.R. Pavlyukova, *Direct numerical simulation of the transitional separated fluid flows around a sphere and a circular cylinder.*, Journal of Wind Engineering and Industrial Aerodynamics, pp 341-358 ,2002